

Tip Vortex Field Resolution Using an Adaptive Dual-Mesh Computational Paradigm

Nathan Hariharan
CREATE-AV, Patuxent River, MD

Andy Wissink
US Army/AFDD, Ames Research Center, Moffett Field, CA

Michael Steffen
CREATE-AV, Patuxent River, MD

Abstract

This paper describes the efforts to model vorticity laden flowfields using the CREATE-AV Helios platform. Helios employs a dual-mesh paradigm: near body unstructured grids, and high order accurate off-body Cartesian grids, and information exchange is facilitated by an automated, implicit hole cutting method. Further, an automatic mesh refinement capability is employed to refine regions of intense vorticity. Two different scenarios are considered: (a) the vortical flow field off a high-angle-of-attack aircraft, (b) the helical wake of a model rotor in hover. The ease of use, efficiency, and power of the Helios dual-mesh paradigm is demonstrated through high fidelity solutions for the aforementioned unsteady, vortical fields.

1. Introduction

1.1 Background

Vortical wakes introduce important aerodynamic phenomena in certain classes of aerospace vehicles. Rotary-wing vehicles, in particular, fly in their own wake and experience numerous aerodynamic effects, affecting vehicle handling qualities, vibration, and noise. The wake of the vehicles also complicates near-ground operations, from shipboard landings to "brownout" conditions in desert flight. Fixed-wing aircraft also experience problems such as tail buffet[1] from tip vortices emanating from the nose and swept wing in high angle-of-attack fighter jets. The availability of accurate and efficient computational models to better predict vortex wake behavior could help to minimize the onset of these sometimes disastrous phenomena.

High-fidelity Reynolds-Averaged Navier-Stokes (RANS) CFD methods have demonstrated the ability to give accurate predictions of aerodynamic loads, but their ability to predict the wake is often limited by numerical dissipation. This can be mitigated by using very fine grids in the wake, but this quickly exhausts available computational resources. For problems where key solution features, like tip vortices, occur only in localized regions of the computational domain, spatial adaptive mesh refinement (AMR) can be an effective tool. AMR involves automatically refining and coarsening the grid locally to resolve important flow features. By focusing memory

usage and computational effort in these localized regions, a highly resolved solution may be obtained much more efficiently than a globally refined grid of equal resolution.

The use of AMR has been studied extensively for wakes of hovering rotors. Strawn and Barth[2] first demonstrated the concept using AMR in an unstructured Euler solver. Potsdam[3] also applied unstructured AMR to wind turbine wake predictions. Deitz et al. [4] introduced an overset-grid based approach that moved tubular curvilinear grids to align with the tip vortices. Hariharan [5] used Cartesian overset vortex-grids to analyze tip vortex from wings. Meakin[6] proposed a Cartesian-based AMR scheme within the Overflow[7] code. This approach was recently extended by Holst and Pulliam[8,9]. The aforementioned efforts all adopted AMR techniques targeting steady-state solutions; a solution is computed on an initial mesh, the mesh is reconstructed to adapt to features in the solution, then the simulation is run again on the new mesh. This steady-AMR approach is useful for isolated rotors in hover conditions, but many of the more complex problems in rotorcraft require time-dependent moving body capabilities. An AMR scheme that can resolve unsteady effects like rotor-fuselage interactions or rotor vehicles in forward flight or maneuver conditions requires an unsteady-AMR approach, for which the grid is adapted continually in a time dependent manner throughout the simulation.

Another important strategy for CFD-based wake resolution is the use of high-order numerics. High-order schemes are effective because they resolve features like tip vortices with much fewer points across the vortex core, so it is possible to achieve better resolution of the vortex wake with a coarser mesh. The benefits of high-order schemes for rotor wakes have been shown by Hariharan[4,10], Sankar[11], Yeshala[12] and Duque et al.[13]. Cartesian grids offer the most computationally efficient approach to high-order accuracy. Unlike Discontinuous Galerkin schemes on unstructured grids, which can be as much as an order of magnitude more expensive than standard second order schemes, finite-difference-based high-order schemes on Cartesian grids are only marginally more expensive than a second-order scheme.

1.2 CREATE-AV Helios Computing Platform

Helios is a new computational platform under the CREATE-AV umbrella targeted towards Aeromechanics simulations. Details of the underlying platform design, validation cases, and targeted applications can be found in Reference [14]. At the heart of the Helios platform is an innovative dual-mesh paradigm with an unstructured mesh solution in the near-body, and Cartesian meshes in the off-body and using automated overset information exchange as a means of communication. The unstructured near-body solver facilitates ease of grid generation for complex body shapes, and the solution is computed using the second-order accurate flow solver NSU3D [15]. The off-body Cartesian grid generation is automatically done using SAMRAI [16]. Cartesian grid infrastructure, and employs an efficient fifth-order spatially accurate solver, SAMARC [17].

The Helios platform deploys overset hole cutting using an implicit methodology [18] that does not require any user interference. The overset connectivity is handled by PUNDIT [19], and the entire process supports parallel/distributed computation. Figure 1.1 illustrates the various

components of the Helios platform. Further, the SAMRAI infrastructure supports the ability automatically to perform Cartesian refinement and adapt to geometric and flow features. The CREATE-AV release of Helios (named “Whitney”) does not support the automated refinement functionality, but the 2011 release (“Shasta”) will officially support the feature.

In this paper, the application of the Helios dual-mesh paradigm –with automated adaption- is explored for resolving two-different vorticity laden flow fields: (i) Aircraft high-AoA vortex system, (ii) Wake vortex system of a rotor-blade in hover.

2. High Angle-of-Attack Aircraft Flowfield

2.1 Baseline Solution

Effects of aerodynamic vortex-shedding impinging on the tail empennage typically occur during maneuvers at high angles of attack (AoA) ranging from 15-25 degrees. A range of such cases were first simulated for an AV-8B aircraft geometry using USM3D - a widely used, second-order, unstructured flow solver. Details of the geometry and the unstructured grid are described in Reference [20]. Figure 2.1a-d shows vorticity contours at several streamwise sections across the aircraft at a twenty degree angle of attack. Clearly, several geometric features feed the vortex generation process. Figure 2.1e shows vorticity iso-surface of the wing-vortex system. The vortices are seen to be largely dissipated by the time it reaches the tail structures. Inadequate grid density distributions and lower spatial order of accuracy of computations contribute to the dissipation. Typically a second order accurate flow solver would require 20-30 points across the core of the vortex to numerically convect the vortices without dissipation. In this context there are several impediments in using a computational strategy as this as a means for engineering predictions of buffet drivers, for a large range of flight conditions.

- i. Global refinement over the entire aircraft providing 20-30 grid points across all the vortices produced over the aircraft will result in untenable number of grid points for engineering computations.
- ii. Targeted unstructured refinements to vorticity and gradients may work if automated, but has historically been proven difficult to achieve without a good deal of expertise in controlling the refinements. Moreover, even with targeted refinements, it is difficult to provide ~30 grid points across the path of the evolving vortices when second order accurate computations are employed.

2.2 Helios Overset Simulation

Next, the same simulation was attempted using the Helios dual-mesh paradigm. The process involved providing the original unstructured mesh to the Helios infrastructure, and allowing it to arrive at the background meshing, and all the required interfaces. Figure 2.2a,b show the side, and front sectional view of the dual-mesh. As can be seen in Figure 2.2a, the finest off-body mesh uniformly covers the expected path of the aerodynamically generated vortices.

Figure 2.3a-d shows directional vorticity contours over a number of streamwise sections along the length of the aircraft, similar to Figure 2.1. The vorticity content generated over the fore-part of the aircraft is much better preserved by the fifth-order off-body Cartesian-grid solution, and a richer, stronger vortex field impacts the empennage. Figure 2.3e shows iso-vorticity contours colored by w-velocity over the entire aircraft, similar to Figure 2.1e, and shows in considerably more detail the computed vorticity field, including the wing-tip vortex.

2.3 Helios Simulation with Cartesian Off-body Grid Refinement

In the simulation described in Section 2.2, the total number of off-body Cartesian points is fixed at the beginning of the simulation at a given fine level. In this section the ability to selectively refine off-body grids to geometric features, and flowfield vorticity is explored. This functionality will be a feature of the 2011 Helios Shasta release. In this simulation the resolution of the finest off-body grid is not specified apriori, but Helios automatically determines the finest grid levels.

Vorticity magnitude is computed on the Cartesian grid by SAMARC. Any cell with vorticity greater than a specified magnitude is tagged for refinement. On the next refine step these tagged cells are clustered to form a new Cartesian block with one level finer (2X) resolution. This process continues until the specified maximum number of levels is reached. An issue with this approach is that careful tuning is required to control mesh size. If the threshold vorticity chosen is too large, no cell in the wake is tagged for refinement. If it is too small, too many cells may be tagged causing the problem size to exceed available computational resources. A new approach [21] that avoids the need for user tuning is currently being tested and is planned to be part of the future release of Helios.

The Automatic Mesh Refinement (AMR) case used the same near-body mesh used in the fixed-refined case (5.55M nodes). Each new finer level in the Cartesian grid framework has double the resolution of the underlying coarser level. The refinement is isotropic, i.e., all three axes are refined. The AMR case uses one level finer grid resolution than the fixed-refined case shown earlier. The case was first run with refinement applied to the problem geometry (i.e. no solution refinement) in order to dissipate non-physical startup transients. It has been found from past calculations that the AMR scheme attempts to track and preserve the startup transients if it is turned on at initialization, and it is helpful to first converge a solution on the geometry-refined mesh before turning on solution-based refinement. The geometry-refined off-body mesh system contained 12.7M off-body nodes, the time/step for the dual-mesh calculation was 3.61sec on 64 processors, with 75% of the total time spent in the near-body solver (NSU3D) and 25% of the time in the off-body solver (SAMARC). Figure 2.4a shows a cross-section of the grids showing the near-body, and off-body grids if Helios is allowed to adapt the off-body Cartesian grids based on the geometric features, and near-body grid resolution. The difference between the off-body Cartesian grid structures of the current simulation, and the simulation described in Section 2.2 can be seen by comparing Figures 2.2 and 2.4a. In Figure 2.4a, the finest levels mesh is adapted to the geometry and is not uniformly fine over a region covering the entire aircraft as in Figure 2.2. Figure 2.4b shows the evolving vorticity field with only the geometry based adaption active.

Initially, the geometry-refined solution was converged. Then the case was run further with the vorticity based solution refinement turned on. Mesh adaptation takes place every 250 steps, totaling 40 adapt cycles over the simulation. The final mesh system at the end of the simulation

contained 20.0M off-body nodes, the time per step is 4.18 sec on 64 processors, with 68% of the time spent in the near-body solver (NSU3D) and 32% in the off-body solver (SAMARC).

Figure 2.5a-c shows several streamwise sections of the refined Cartesian grid along the length of the aircraft. The grid refinement is seen to track the approximate evolution of the vortices generated. Figure 2.6a shows vorticity contours overlaid with the refined grid at a spanwise section along the wing. The vorticity transported from the near body solution near the wing is convected in the off body grid all the way to the empennage, with no noticeable loss due to the localized refinement of the Cartesian grid.

Figure 2.6b shows iso-vorticity contours colored by w-velocity over the entire aircraft, similar to figure 2.3e. The richness of the vorticity field in the vicinity of the empennage sections is remarkably well captured without any noticeable dissipation – due to a combination of 5th order special accurate algorithm and adaptive provision of enough Cartesian grid points across the path of the vortex structures. Figure 2.7 compares the second order, the fixed Cartesian, and AMR Cartesian solutions. The AMR Cartesian solution provides detailed resolution of the high-AoA vortex field for a marginal increase in the cost of CPU/time step (Unstructured only: 3.83 sec/iter to AMR Cartesian: 4.18 sec/iteration). A central advantage in this approach is the ability of the method to automatically adapt the background Cartesian grid with changing flight conditions without having to go back and regenerate the near-body unstructured grid.

Figure 2.8 shows the unsteady pressure imprint of the fore-body generated vortical flowfield on the vertical tail. The unsteady excitation can be fed to a structural solver to analyze fatigue response. Figure 2.9 show vorticity iso-surface of the flowfield being captured several body lengths behind the aircraft, when the Cartesian adaption is allowed to refine further. Such an ability to preserve vortical fluctuations over multiple-aircraft lengths will be very useful to study interactional aerodynamics of multi-aircrafts in flight (i.e., mid-air refueling, close-proximity flights, impact of engine jet-exhaust etc.).

3. Vortex-wake of a Rotor in Hover

A substantial portion of this study also focused upon the physics and numerics of computing the vortical wake of a rotor in hover. The Caradonna-Tung [22] rotor-blade - a two bladed rotor model tested in 1981- was used to explore several aspects of predicting hover using Helios. The blade planform consists of untwisted, non-tapered NACA0012 sections with an aspect ratio of 6. An unstructured blade grid was generated using AFLR3 volume grid generator.

3.1 Out-of-Ground Hover

To initiate the calculations the blade grid was set in a prescribed Cartesian grid setting. The finest grid level was initiated at 9-grid-cells per chord (referred to as Level-5 grid). The background Cartesian grid was intentionally solved employing a second-order spatially-accurate method. The Helios code was run in the rotational-mode. The run collective pitch was set at 8 degrees, and the tip Mach number was 0.44. The blade grid had 3.3 million grid points, and the coarse, Level-5 off-body grid had 2.2 million grid points. Figure 3.1 shows vorticity contours across a chordwise-cross section in the middle of the middle of the blade. The tip vortex

originates in the blade-grid, and transfers to the Cartesian grid. The large amounts of diffusion associated with the second-order scheme and coarser Cartesian grid causes the vortex system to settle-down to a ring-state within a single-revolution. As the computation proceeds, the solution arrives at a numerically stable vortex structure as seen in figure 3.2. The presence of the cumulative vortex ring so close the rotor-blade results in much larger induced flow, and hence a much lower predicted thrust coefficient of 0.003118 (experimental thrust coefficient = 0.0046).

The background Cartesian grid finest-level resolution was doubled to 18-grid-cells per chord (referred to as Level-6 grid). The off-body Cartesian grid count was 22.5 million. Figure 3.3(a, b) shows similar vorticity magnitude contours, and vorticity iso-surfaces (colored by z-velocity) with the computational order of accuracy in the Cartesian grid still being retained at the second-order level. The wake system evolves below the vortex further down before being consumed by the ring-vortex. Figure 3.4 shows on vorticity iso-surfaces focusing on the structure of the wake-sheet. The helical wake sheet system that descends faster than the tip-vortex system is seen to be well captured.

Figure 3.5 shows wake vorticity contours when the computational order of accuracy of the Cartesian grid was increased to 5th. The wake vortex system is sharply defined with the vortex-ring structure pushed further down, but persisting in the eventual converged solution. Figure 3.6 (a,b) show two different views of helical tip vortex structure using iso-surfaces in the wake (colored by z-velocity). The helical system convects down due to its own self-induced velocity, but eventually rolls up into a toroidal vortex ring. Figure 3.7(a) shows vorticity iso-surfaces of both the computed tip-vortex, and the wake-sheet systems. Figure 3.7(b) shows the well-known idealized schematic of a rotor-wake. The agreement between figures 3.7(a) and 3.7(b) is striking. The computed thrust coefficient converged to a value of 0.0052, approximately 10% higher than the experimental value.

There are several possible reasons on why the thrust comes out higher: (i) accuracy of the near-body solution, (ii) effect of center-body, (iii) far-field conditions (wind-tunnel vs. free-stream) etc. We explored some of these issues, starting with the near-body solution. In the Helios dual-mesh paradigm, the near-body solution is computed using NSU3D, a second-order spatially accurate unstructured solver. Figure 3.8(a) shows a streamwise cross-section of the baseline near-body unstructured grid (R0: 3.3 million grid points). A grid refinement tool developed by the CREATE-AV Kestrel team was used to refine the tip region of the rotor-blade grid. Figure 3.8(b) shows the new blade grid (R1: 8.3 million grid points), refined to double the grid density in the tip region. The resulting solution improves the resolution of the tip vortex formation over the blade-tip. Figure 3.9(a, b) compares the tangential peak-to-peak velocity across the tip-vortex at a streamwise station near the blade trailing edge, between the Level-0, and Level-1 grid solutions. The peak-to-peak tangential velocity magnitude from the Level-1 simulation is approximately 30% more than the Level-0 value. Figure 3.10 compares resulting wake vorticity in the Cartesian grid between the two simulations (R0: colored by z-velocity, R1: black grid surface), and no significant difference in the wake location is noted. The computed thrust coefficient from the R1 simulation converged to a value of 0.0050, trending towards the experimental value.

Concurrently, the study started focusing on automated mesh refinement (AMR) of the Cartesian solution. In the AMR method, a maximum adaption cell size, and a minimum vorticity threshold to adapt to are prescribed. Figure 3.11 shows vorticity contours, and the resulting grid for a vorticity threshold of 0.005, and maximum grid level of 6 (18 cells per chord). The vorticity threshold is small enough to include refinement in the entire wake. Figure 3.12 compares the wake vortex peak-to-peak strength at several azimuthal angles ($\Psi=30, 210, 390, 570$ degrees). The number of nodes the peak-to-peak variation is captured is plotted for each of the azimuthal angles. The strength drops off from $\Psi=30$ degrees where the vortex is captured with ~ 9 cells till the point it spreads to ~ 12 cells across ($\sim \Psi=210$ degrees), and thereafter maintains the resolution. This is in line with expectations for a fifth-order spatially accurate scheme. Further off-body refinement work is in progress.

It is instructive to compare the current simulation from an earlier, 7th order spatially accurate, overset grid simulation by Hariharan and Ekaterinaris [23] using the NSHOCS code. Figure 3.13(a) shows a near-body C-grid, and off-body clustered Cartesian grid. The solution was run in a fully transient mode, for the same flow conditions, and both near and off-body grids were computed using a ENO-based 7th order accurate scheme. Figure 3.13(b) shows the wake vortex structure, and the simulation predicts a similar vortex ring as seen in the current Helios simulations. Figure 3.14 shows tangential peak-to-peak variations across various tip-vortex azimuthal locations. The peak-to-peak values compare similar to the Helios wake structure in figure 3.12. However, the computed thrust coefficient in the Hariharan and Ekaterinaris [23] simulation was reported at a value of 0.00462 – very close to the experimental thrust coefficient. The only substantial difference between the NSHOCS simulation and the current Helios simulation is the computational accuracy of the near-body computation. Coupled with the fact that the R1 Helios solution trended in the right direction compared to the R0 Helios solution, it is quite suggestive that the near-body flow solution accuracy (especially the creation of the tip vortex and its evolution over the wing) plays a large role in closing the last 10% gap in computed vs. experimental loads. In Helios, this increase in near-body tip-flowfield accuracy could be achieved either by further near-body tip-grid refinement, or adding a higher-order structured/strand grid near-body solution option – both of which are in the works for future releases.

Thus far, all the rotor-wake simulations presented in this section utilized the steady hover formulation, which uses a fixed grid with rotational source terms applied to the equations solved on the grid, and is usually accepted as a good approximation for isolated hover predictions. However, problems involving rotor-fuselage interactions, multiple rotors, or helicopters in forward flight which are ultimately of interest to helicopter engineers require an inertial formulation with moving grids capable of simulating bodies in relative motion. A useful validation is an investigation into whether the two formulations -- steady hover vs. inertial hover -- give the same answers. Figure 3.15a shows the tip vortex wake structure from an inertial simulation (R0 near-body, L6-Level Cartesian, 5th order accuracy in the Cartesian), and it exhibits the helical structure feeding a persistent vortex ring similar to the rotational solution. Figure 3.15b plots the tip-vortex iso-surfaces for the inertial (colored by z-velocity) and the earlier rotational solution (grayscale). The vortex-ring stands off at a slightly different z-location, and the helical vortex structure z-locations vary a bit after the wake azimuthal angle exceeds 360 degrees. However, the net thrust coefficient levels for the inertial simulation converge to a value

of 0.00518, close to the rotational mode predictions. Further, a tear-drop shaped center-body was inserted into the simulation. Figure 3.16 shows the tip vortex of the resulting system. No major changes were observed either in the vortex structure or the resulting integrated thrust.

3.2 Near-Ground Hover

The Caradonna-Tung rotor-blade configuration was then used to study if Helios can reproduce the beneficial effects on thrust and efficiency when hovering near-ground. Figure 3.17 shows the vorticity contours of the wake when the rotor-blade is hovering at 0.5 rotor radius above the ground. Inviscid wall conditions were set at the lower boundary of the Cartesian box. The vortex system flares out (consistent with ground image vortices), and the vortex ring is pushed out further. Figure 3.18 shows vorticity iso-surfaces at different levels to “see-through” the complex vortical structures near the ground. Figure 3.18(a) – high iso-vortex level – shows the internal structure of the tip vortices feeding the flared out toroidal ring vortex. Figure 3.18(c) – low iso-vortex level – shows the radial location of the ground effect roll of the entire wake tip-vortex, and wake-sheet. Figure 3.18(b) – medium iso-vortex level is the most interesting - shows formation of intense braided vortex structures around the ring-vortex enhancing mixing in all directions. A well-known operational issue of hovering/landing near a dusty-ground is the “brownout” phenomena, where dust-particles mix so thoroughly to reduce pilot visibility quickly to near-zero levels. The vortex structure in figure 3.18(b) begins to explain why the dust transport mixing is so thorough and fast. Figure 3.18(b) shows a flared out toroidal ring vortex braided by secondary small-scale vortices forming rings all around the circumference. Such a vortex structure enhances mixing across scales, and hence aids quick and uniform distribution of dust particles that are picked up from the ground surface. Figure 3.19 shows streamline contours (colored by velocity magnitude) of particles seeded near the ground surface. The high level of internal mixing –near the ground- distorts the classical solenoidal flow field of free flight hover.

Figure 3.20 compares the vortex strength evolving off the blade between free flight (a) and near-ground flight (b). The vortex strength reduces on theoretically expected lines implying higher predicted hover efficiency near the ground. Figures 3.21 compares similar vorticity contours, and figure 3.22 compares similar near-ground seeded particle streamlines when the hover distance is increased to 0.625 times the rotor diameter. The flow-field begins to tend towards a free-flight hover mode. Figure 3.23 plots the near-ground to out-of ground thrust ratios computed by Helios for these two locations, and compares it with historical data, and an image-vortex theory based predictions (figure reproduced from Leishman [24]). The Helios simulations predict near-ground thrust gains that conform to image-vortex theory.

5. Conclusions & Recommendations

This paper describes the efforts to model vorticity laden flowfields using the CREATE-AV Helios platform. Helios employs a dual-mesh paradigm: near body unstructured grids, and high order accurate off-body Cartesian grids, and information exchange is facilitated by an automated implicit hole cutting method. Further, an automatic mesh refinement capability within Helios was employed to refine regions of intense vorticity. Two different scenarios were considered: (a) the vortical flow field off a high-angle-of-attack aircraft, (b) the helical wake of a model rotor in

hover. The ease of use, efficiency, and power of the Helios dual-mesh paradigm was demonstrated through high fidelity solutions for the aforementioned unsteady, vortical fields.

The geometric complexities of a full-up aircraft with all the associated pylons, and missiles, and pods require flexible and efficient CFD simulation tools that utilize unstructured meshes. One of the charters of CREATE-AV is to propagate the use of Computational Based Engineering (CBE) to non-CFD experts, and therefore the process utilized to arrive at the solution cannot be too dependent on fine-tuned expertise of the user. Hence the right process to arrive at a good-quality engineering solution becomes equally important.

A combination of Helios capabilities - (i) to compute 5th order spatial accuracy in the Cartesian grids, and (ii) to automatically refine the Cartesian grid to vortical flow features - enabled accurate convection of the vortex structures hitting the empennage. A central advantage in this approach is the ability of the method to automatically adapt the background Cartesian grid with changing flight conditions without having to go back and regenerate the near-body unstructured grid. Such an ability to preserve vortical fluctuations over multiple-aircraft lengths will also be very useful to study interactional aerodynamics of multi-aircrafts in flight (i.e., mid-air refueling, close-proximity flights, impact of engine jet-exhaust etc.). Further detailed studies are recommended to validate the Helios methodology by incorporating engine exhaust effects, and coupling the tail unsteady loads to a structural model.

Similarly, the off-body Cartesian solver in Helios resolved the helical tip-vortex and wake sheet of the hover field adequately. The Cartesian grid resolution needs to be of the order of ~ 12 points across the vortex core for propagating the tip-vortex without noticeable dissipation. AMR needs to be further explored to refine just around the helical wake structure. For a blunt tipped blade such as the Caradonna-Tung model rotor, the near-body second-order solver resolution needs further refinement in order to resolve the high tangential and axial gradients across the tip vortex as the vortex forms over the wing. This lack of adequate grid resolution near the blade tip to capture the vortex formation has a definite bearing on the final predicted thrust.

Helios calculations accurately predicted the near-ground hover thrust gains compared to out-of-ground hover. Helios also captured rich details of a flared out toroidal ring vortex braided by secondary small-scale vortices forming rings all around the circumference, and thus provided some insights into the multi-scale mixing process during brownouts. Such a vortex structure enhances mixing across scales, and hence aids quick and uniform distribution of dust particles that are picked up from the ground surface. Helios can potentially be useful for simulating helicopter brownouts, and any strategies to mitigate their effects.

Acknowledgement

Material presented in this paper is a product of the CREATE-AV Element of the Computational Research and Engineering for Acquisition Tools and Environments (CREATE) Program sponsored by the U.S. Department of Defense HPC Modernization Program Office. Dr. Robert Meakin is the program manager for CREATE-AV. The first author would like to thank Mr. Joseph Laiosa (CREATE-AV, NAVAIR 4.3.2.1) for his guidance in the grid generation process, and Dr. David Findlay (NAVAIR 4.3.2.1) for his support.

References

1. Morton, S., R.~Cummings, and D.~Kholodar, ``High Resolution Turbulence Treatment of F/A-18 Tail Buffet," AIAA-2004-1676, 45th AIAA Structures, Structural Dynamics and Materials Conference, Palm Springs CA, 2004.
2. Strawn, R.C., and T.J. Barth, ``A finite-volume Euler solver for computing rotary-wing aerodynamics on unstructured meshes," Journal of the American Helicopter Society, Vol.~38, 1993, pp.61--67.
3. Potsdam, M., and D. J. Mavriplis, ``Unstructured Mesh CFD Aerodynamic Analysis of the NREL Phase VI Rotor," AIAA-2009-1221, 47th AIAA Aerosciences Meeting, Orlando FL, Jan 2009.
4. Dietz, M., E. Karmer, and S. Wagner, ``Tip Vortex Conservation on a Main Rotor in Slow Descent Flight Using Vortex-Adapted Chimera Grids," AIAA-2006-3478, 24th AIAA Applied Aerodynamics Conference, San Francisco, CA, June 2006.
5. Hariharan, N., ``Rotary-Wing Wake Capturing: High Order Schemes Towards Minimizing Numerical Vortex Dissipation," AIAA Journal of Aircraft, Vol. 39, No. 5, pp.~822-830, 2002.
6. Meakin, R.L., ``Automatic Off-body Grid Generation for Domains of Arbitrary Size," AIAA-2001-2536, 15th AIAA Computational Fluid Dynamics Conference, Anaheim CA, June 2001.
7. Buning, P.G., et al., ``OVERFLOW User's Manual, Version 1.8," NASA Langley Research Center, 1998.
8. Holst, T., and T. Pulliam, ``Overset Solution Adaptive Grid Approach Applied to Hovering Rotorcraft Flows," AIAA-2009-3519, 27th AIAA Applied Aerodynamics Conference, San Antonio, TX, June 2009.
9. Holst, T., and T. Pulliam, ``Optimization of Overset Solution Adaptive Grids for Hovering Rotorcraft Flows," 2010 AHS Specialists Meeting on Aeromechanics, San Francisco CA, January 2010.
10. Hariharan, N., and L. Sankar, ``High-Order Essentially Non-oscillatory Schemes for Rotary-Wing Wake Computations," Journal of Aircraft, Vol.~41, No.~2, 2004, pp.~258--267.
11. Sankar, L., N.Yeshala, and N. Hariharan, ``Application of Spatially High Order Adaptive Methods for Unsteady Flow over Rotary Wing Configurations," International Forum on Rotorcraft Multidisciplinary Technology, American Helicopter Society Specialists Meeting, paper No. 21-1, Seoul, Korea, October 2007.
12. Yeshala, N., A.T.Egolf, R.Vasilescu, and L. Sankar, ``Application of Higher Order Spatially Accurate Schemes to Rotors in Hover," AIAA Paper No. 2006-2818, 24th AIAA Applied Aerodynamics Conference, San Francisco, CA, June 2006.
13. Duque, E., L. et al., ``Revolutionary Physics-based Design Tools for Quiet Helicopters," AIAA Paper 2006-1068, 44th AIAA Aerospace Sciences Meeting, Reno NV, Jan 2006.
14. Sankaran, V., et al., ``Application of the Helios Computational Platform to Rotorcraft Flowfields," AIAA-2010-1230, 48th AIAA Aerospace Science Meeting, Orlando FL, Jan 2010.
15. Mavriplis, D.J., and V. Venkatakrishnan, ``A Unified Multigrid Solver for the Navier-{S}tokes Equations on Mixed Element Meshes," International Journal for Computational Fluid Dynamics}, Vol.8, 1997, pp.247-263.
16. Hornung, R.D., A.M. Wissink, and S.R. Kohn, ``Managing Complex Data and Geometry in Parallel Structured AMR Applications," Engineering with Computers, Vol. 22, No. 3-4, Dec. 2006, pp.181-195
17. Wissink}, A.M., Kamkar, S.~J., Sitaraman, J., and Sankaran V., Cartesian Adaptive Mesh Refinement for Rotorcraft Wake Resolution, 28th Applied Aerodynamics Conference, Jun. 2010.
18. Lee, Y., Baeder, J., ``Implicit Hole Cutting – A New Approach to Overset Connectivity, “ AIAA-2003-4128, 16th AIAA CFD Conference, Orlando, June 2003.
19. Sitaraman, J., M.Floros, A.M.Wissink, and M.Potsdam, ``Parallel Unsteady Overset Mesh Methodology for Unsteady Flow Computations Using Overlapping and Adaptive Cartesian Grids," Journal of Computational Physics, Volume 229, Issue 12, June 2010, pp. 4703-4723.
20. Hariharan, N., Wissink, A., Hunt, J., Sankaran, V., ``A Dual-Mesh Simulation Strategy for Improved AV-8B Aft-Fuselage Buffet Load Prediction," AIAA 2010-1234, 48th AIAA Aerospace Sciences Meeting and Exposition, Orlando, FL, Jan 2010.
21. Kamkar, S., et al., ``Automated Grid Refinement Using Feature Detection," AIAA 2009-1496, 47th AIAA Aerospace Sciences Meet, Orlando, FL, January 2010.
22. Caradonna, F.X., and Tung, C., ``Experimental and Analytical Studies of a Model Helicopter Rotor in Hover," NASA TM 81232, 1981.

23. Hariharan, N., Ekaterinaris, J., et al., "An Evaluation of High Order Spatial Accuracy Algorithms for Modeling Fixed and Rotary Wing Tip Regions," AHS Aerodynamics, Acoustics, and Evaluation Technical Specialists Meeting, San Francisco, CA, January 2002.
24. Leishman, G., Helicopter Aerodynamics, Cambridge University Press, 2002.

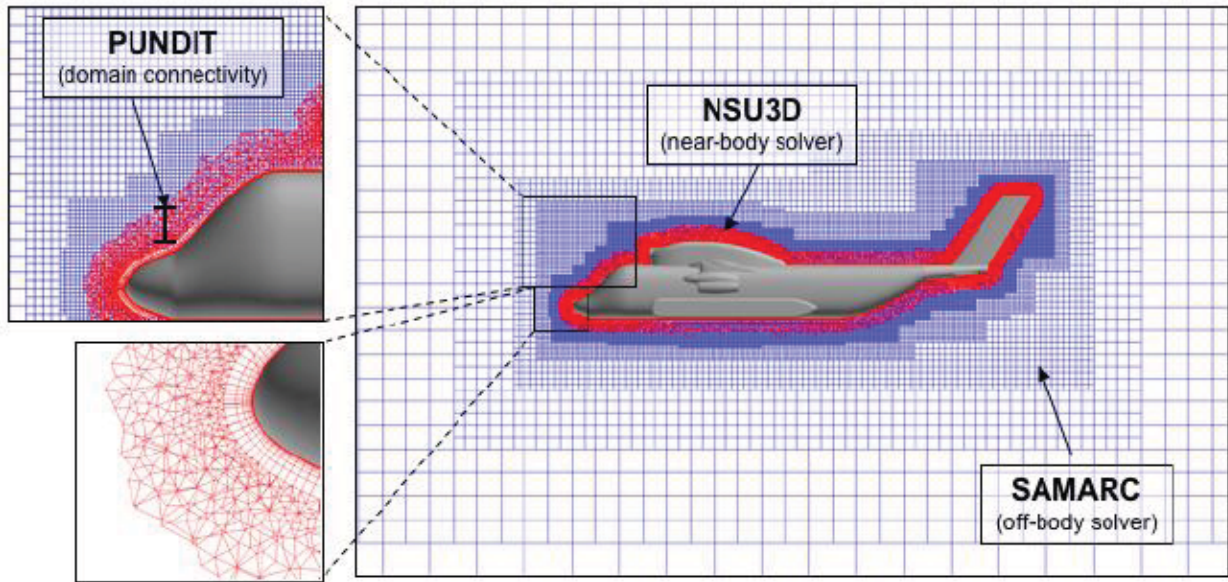


Figure 1.1. Dual-mesh paradigm used in the Helios platform with unstructured near-body grids to capture geometric features and boundary layer near the body surface, and block-structured Cartesian grids to capture far-field flow features.

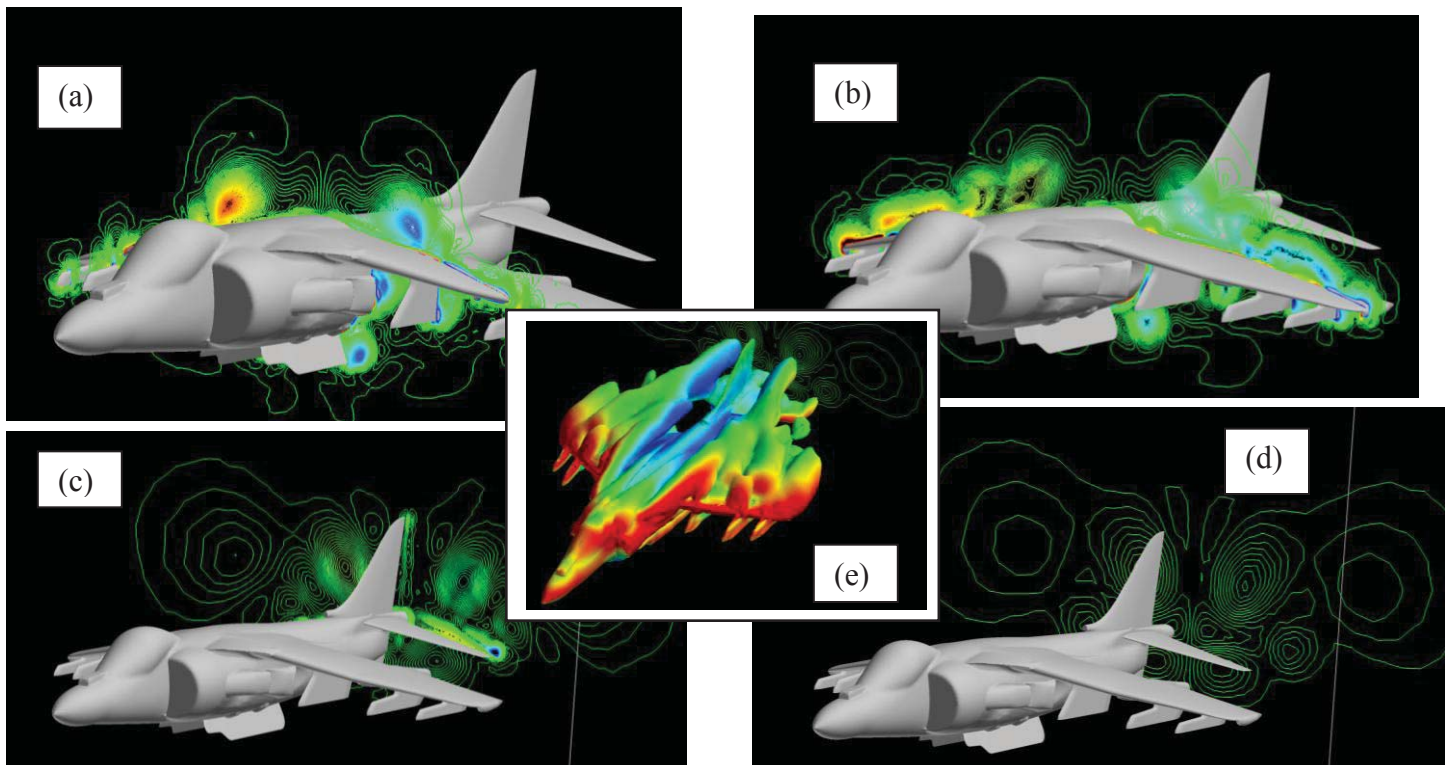


Figure 2.1. (a-d) Directional vorticity contours at several streamwise locations across a AV-8B aircraft configuration. Twenty degrees angle of attack conditions, USM3D simulation. Inset (e): Vorticity iso-surface over the entire aircraft colored by z-velocity.

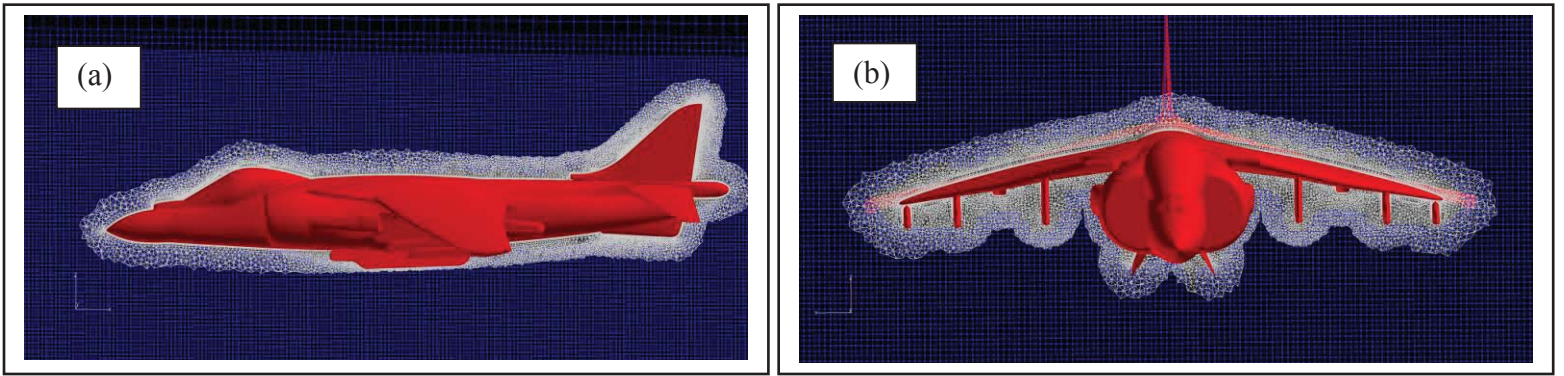


Figure 2.2. Sectional views of coupled near-body (NSU3D) and off-body (SAMARC) computation using HELIOS.

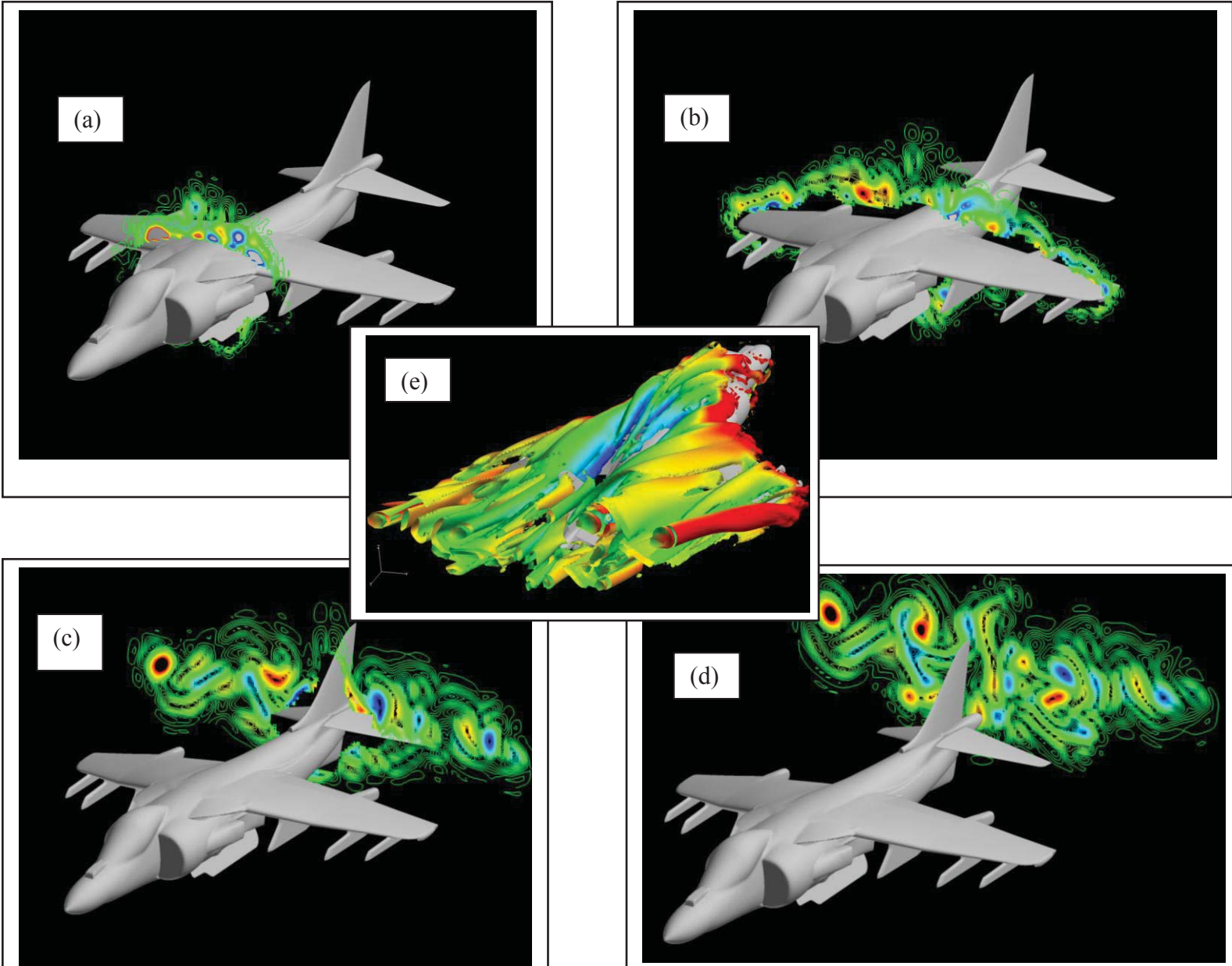


Figure 2.3. (a)-(d) Directional vorticity contours at several streamwise locations across the aircraft. (e) Vorticity iso-surface over the entire aircraft colored by z-velocity. Twenty degrees angle of attack conditions. Computations from composite near-body (NSU3D), and off-body (SAMARC) overset computations under the Helios environment. Off-body solutions is 5th order accurate in spatial resolution.

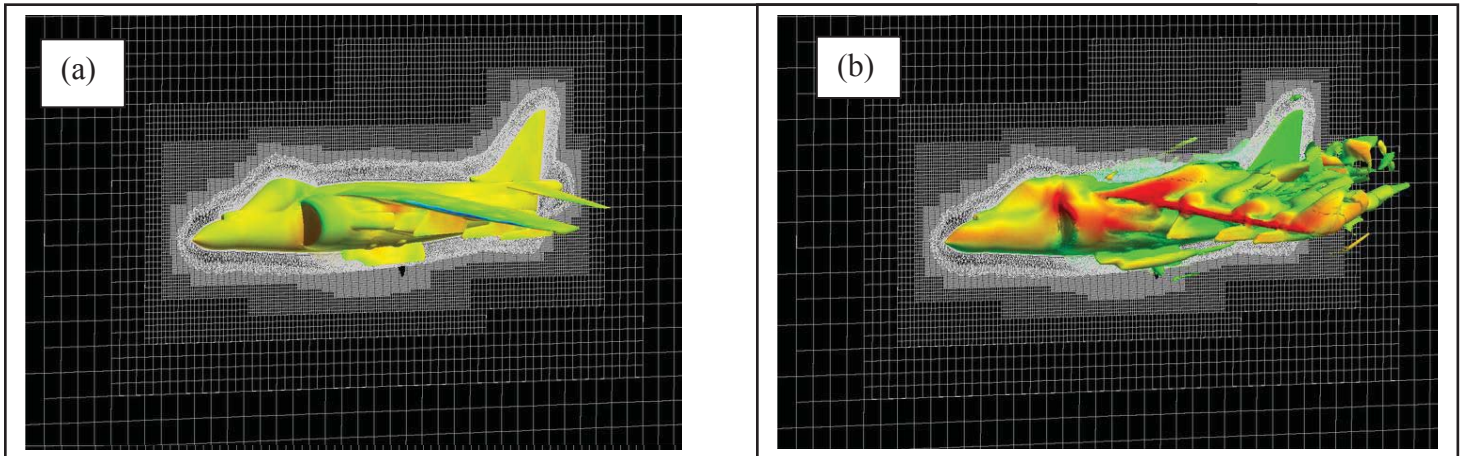


Figure 2.4. (a) Off-body Cartesian grids adapted to geometry by Helios platform. (b) Vorticity iso-surface in the evolving flowfield colored by z-velocity from a first-pass solution prior to flow-based Cartesian adaptation

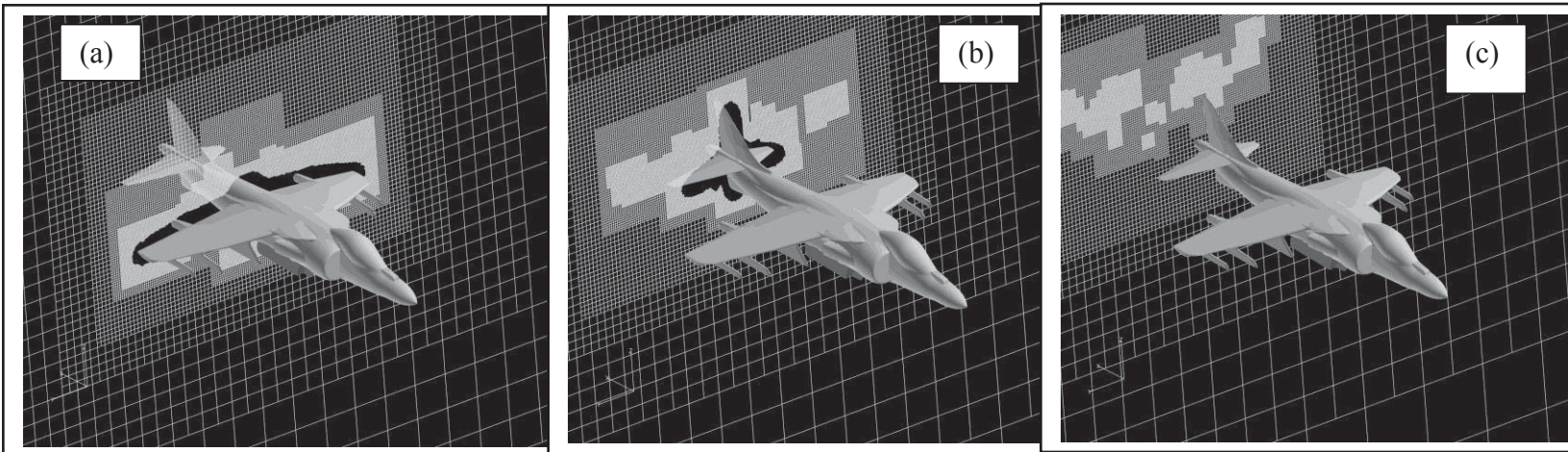


Figure 2.5. Streamwise sectional views of the off-body Cartesian grids refined to track vorticity.

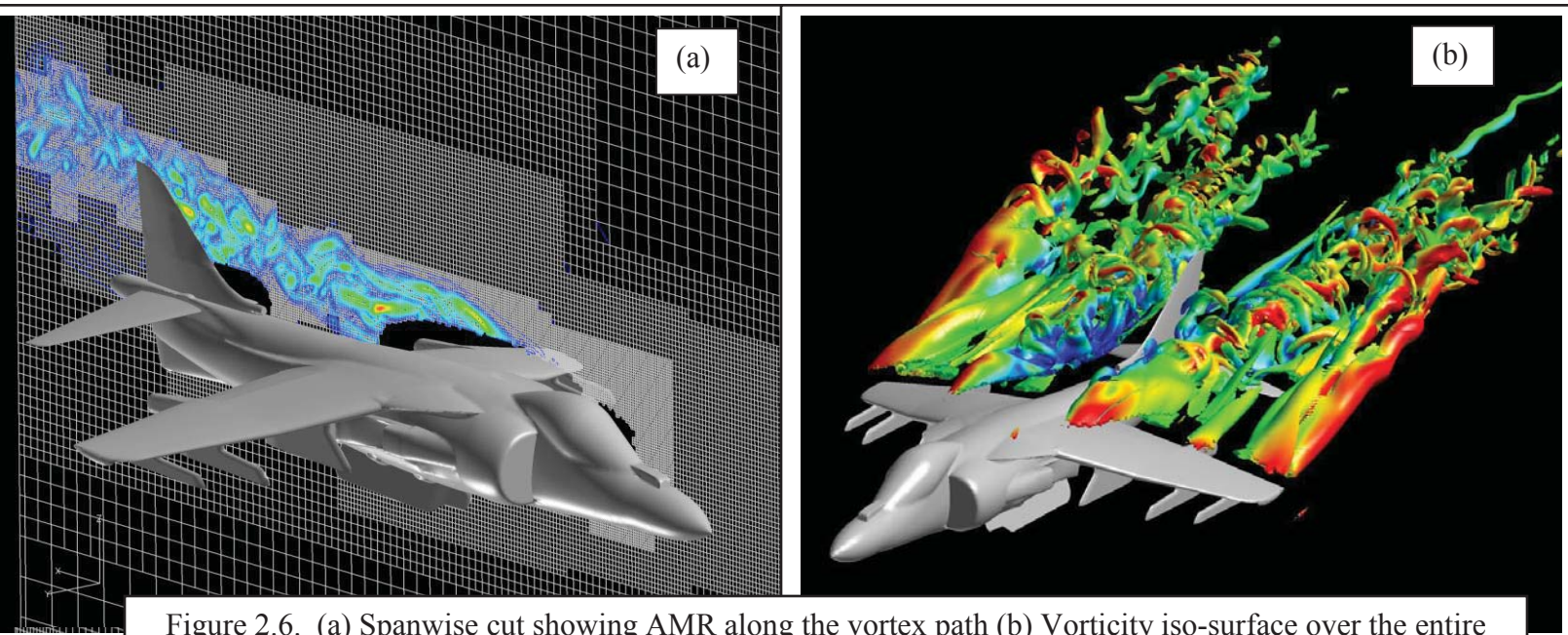


Figure 2.6. (a) Spanwise cut showing AMR along the vortex path (b) Vorticity iso-surface over the entire aircraft colored by z-velocity. Twenty degrees angle of attack conditions. Helios computation employing off-body Cartesian grid refinement (5th order accuracy).

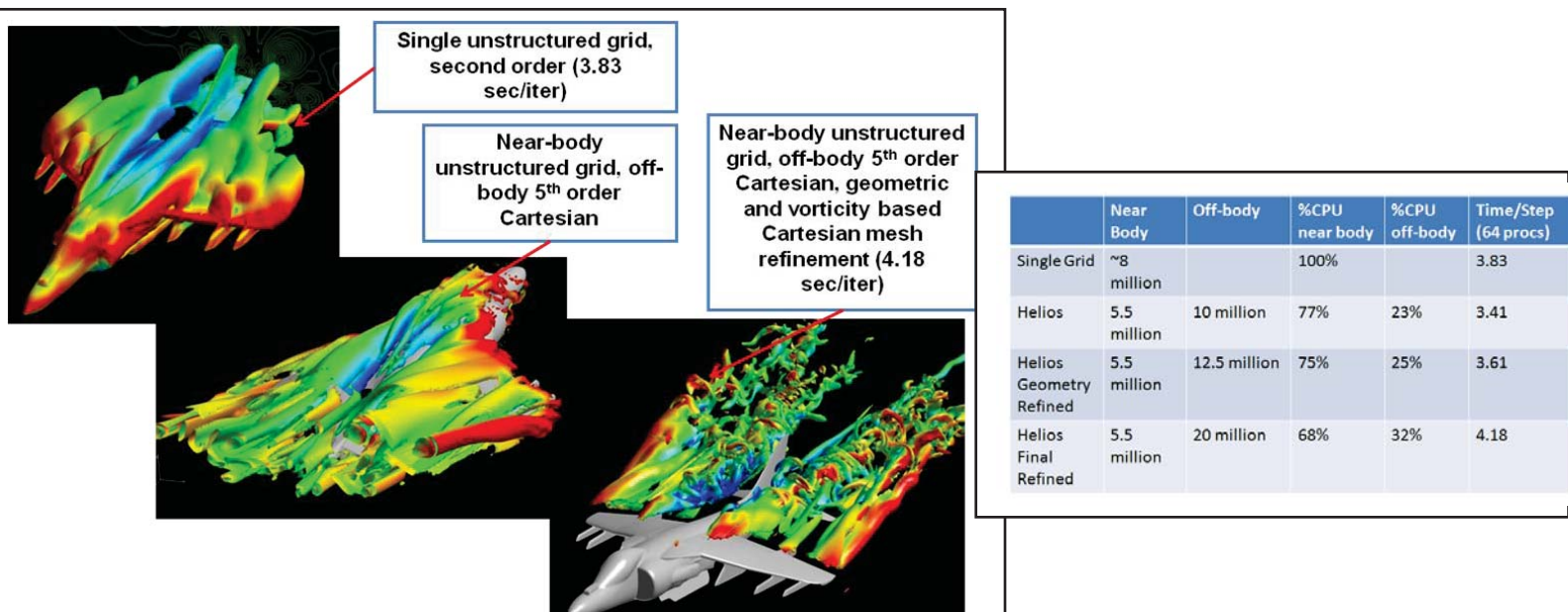


Figure 2.7. Comparison of vortical flowfield resolution, and the time-step per iteration required to achieve the solution between the three solution methodologies.

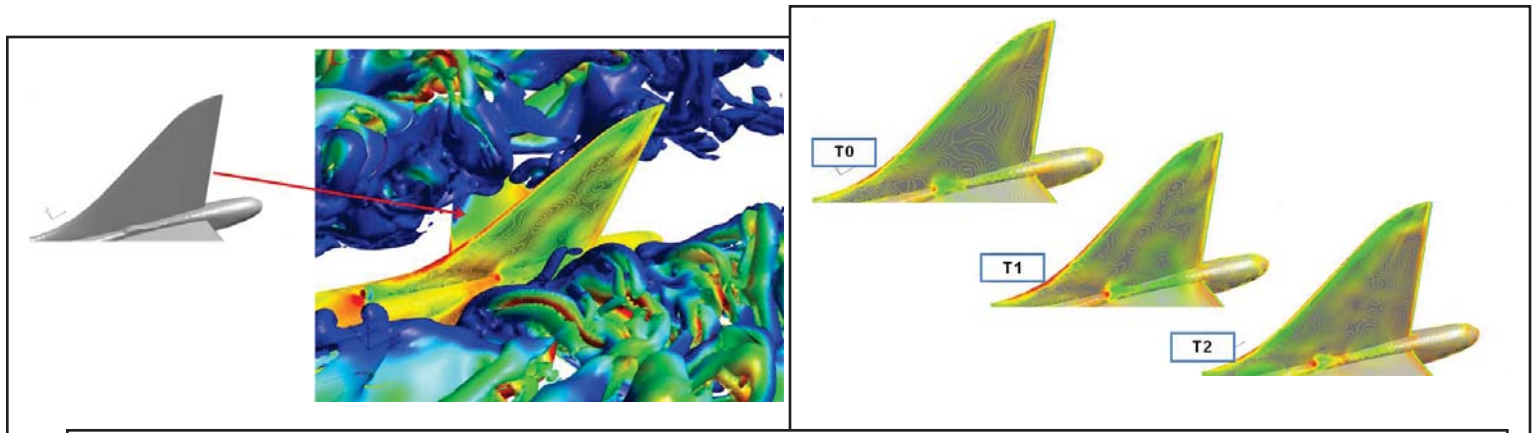


Figure 2.8. Unsteady pressure contours at different time instances on the vertical tail due to the presence of the unsteady vortex flowfield.

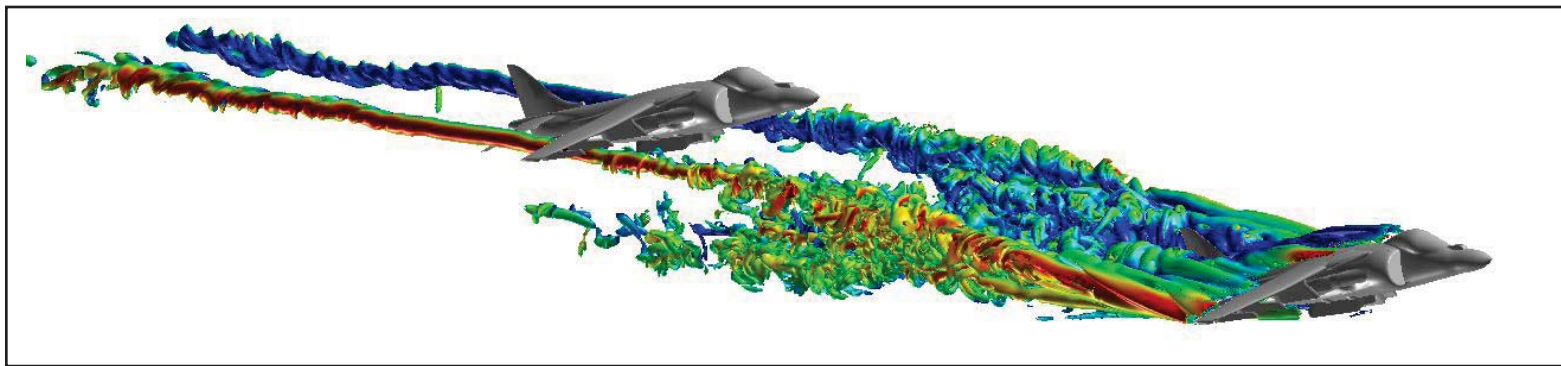


Figure 2.9. AMR based on vortex resolution carried out to multiple-body lengths behind the aircraft. Second aircraft (hypothetical) could potentially be analyzed for interaction effects.

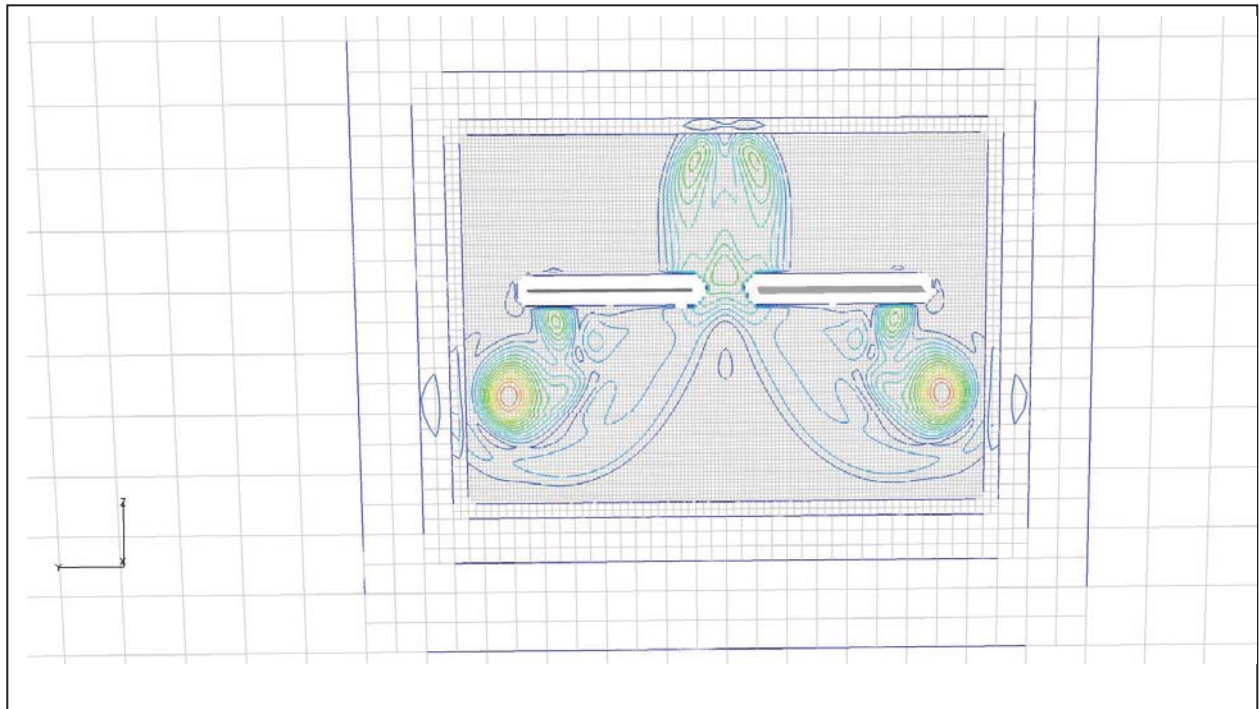


Figure 3.1. Vorticity magnitude contours. Cartesian: Level-5, 2nd Order.

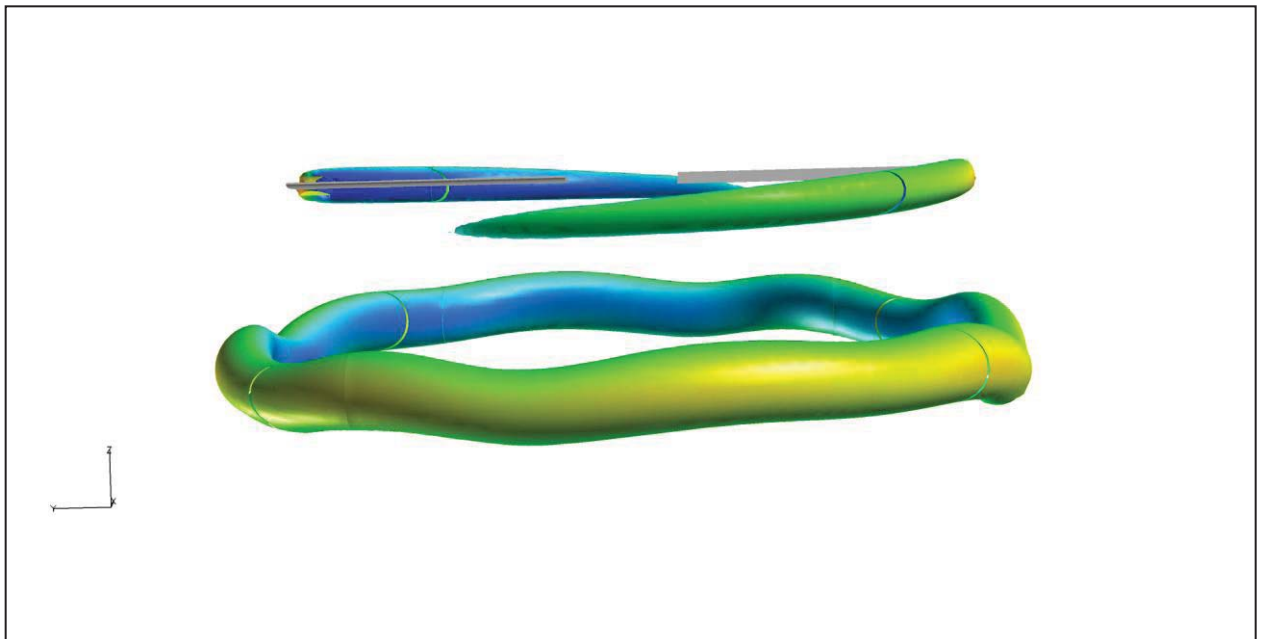


Figure 3.2. Iso-vorticity contours colored by z-velocity. Cartesian: Level-5, 2nd Order.

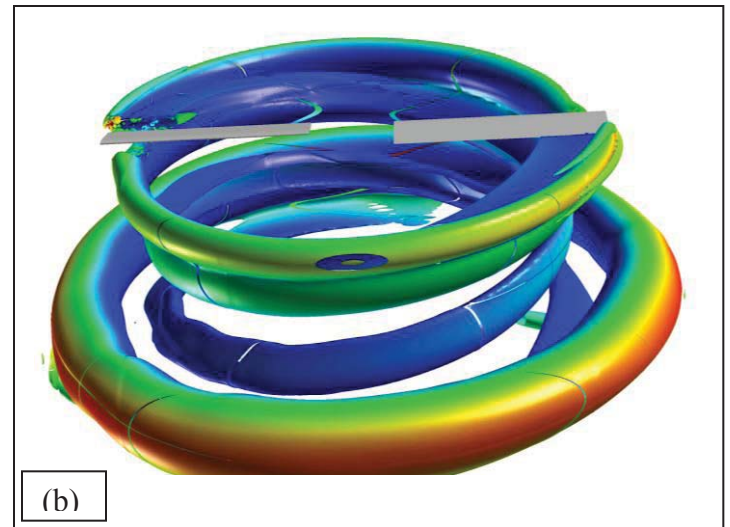
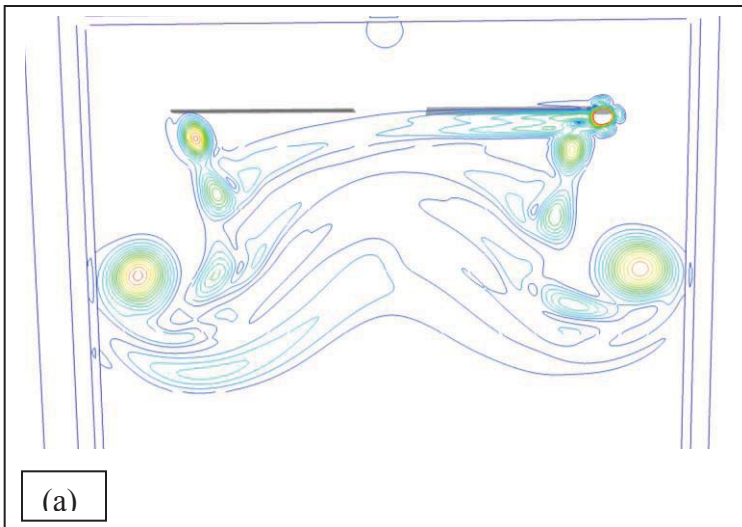


Figure 3.3 . Vorticity magnitude and Iso-vorticity contours colored by z-velocity. Cartesian: Level-6, 2nd Order.

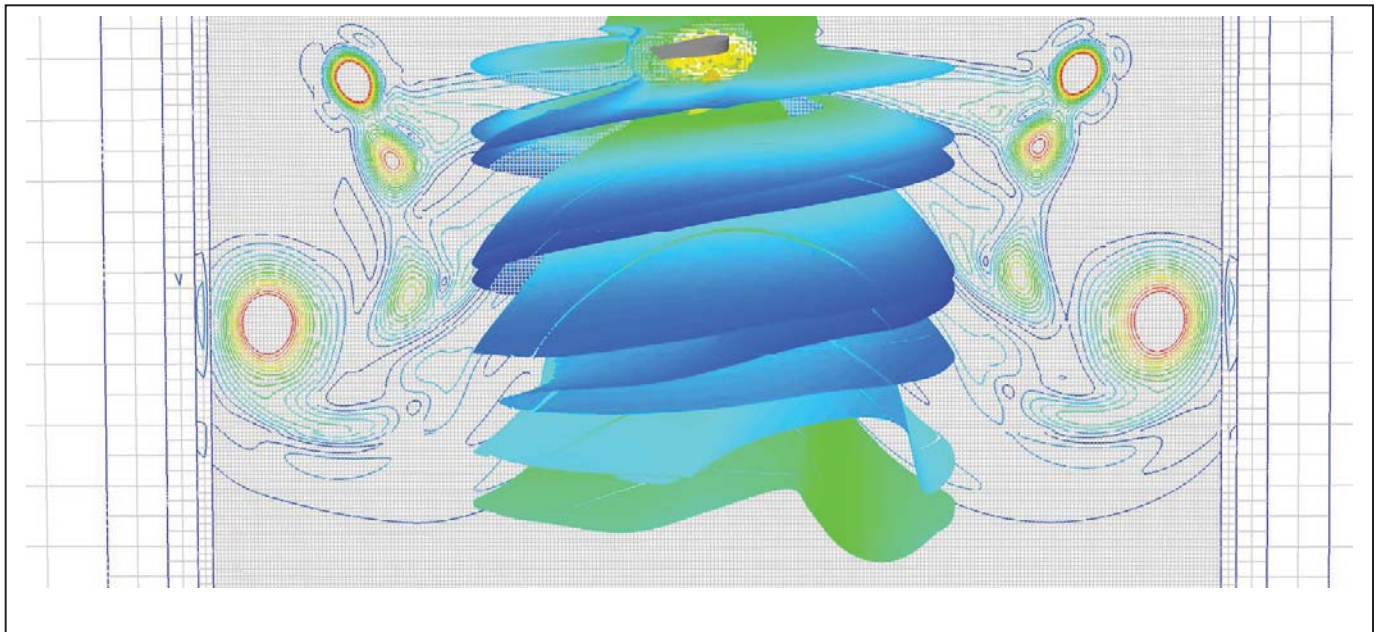


Figure 3.4. Vorticity magnitude and Iso-vorticity contours colored by z-velocity, showing wake-vortex sheet structure. Cartesian: Level-6, 2nd Order.

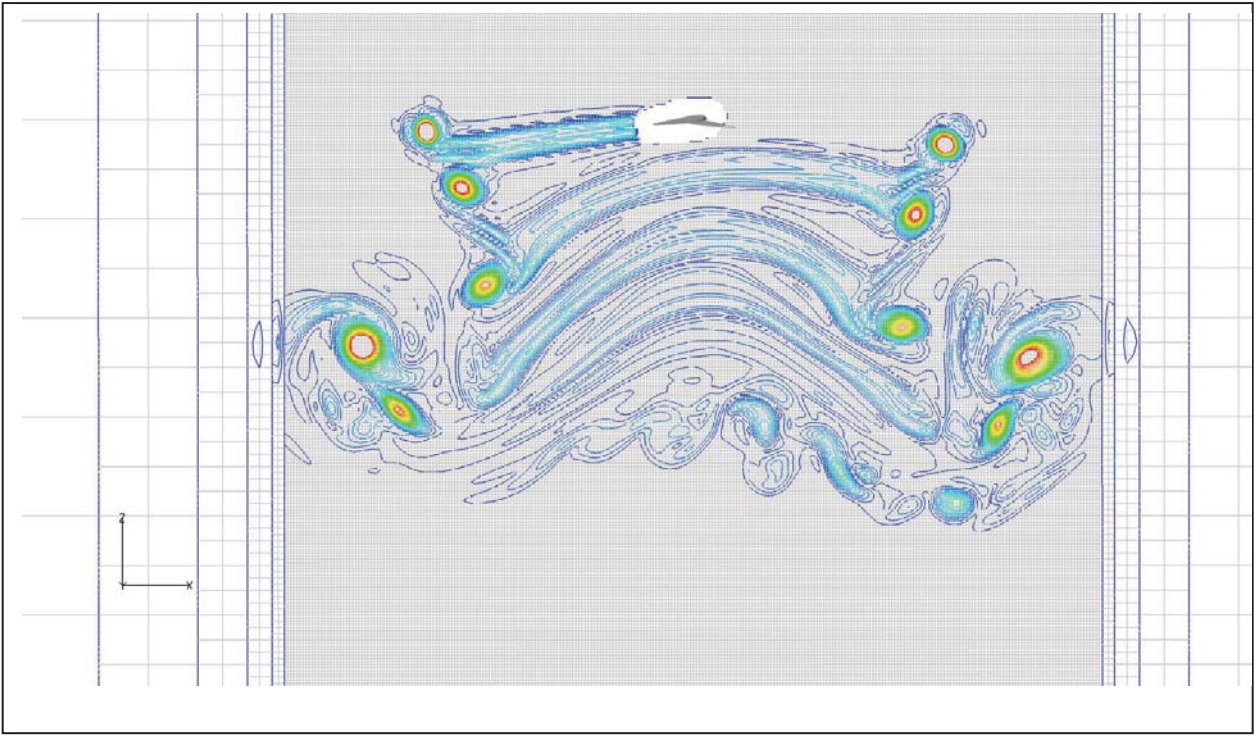


Figure 3.5. Vorticity magnitude contours in the wake, showing wake-vortex sheet structure. Cartesian: Level-6, 5th Order.

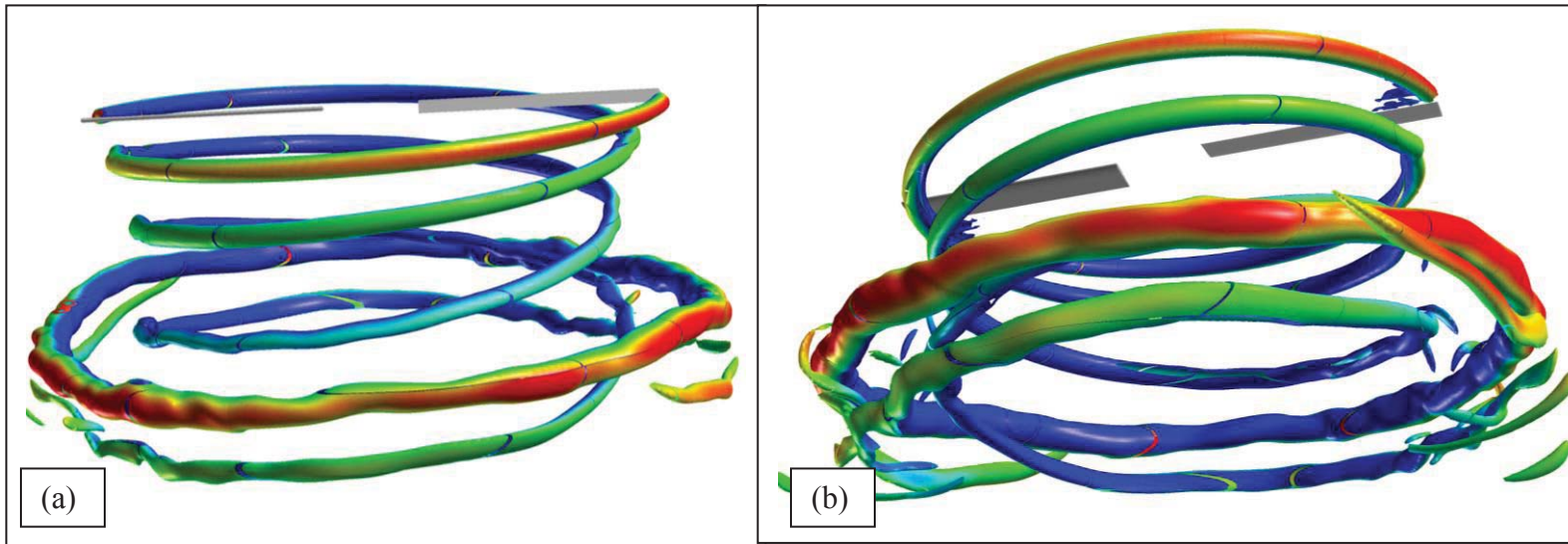


Figure 3.6 . Vorticity Iso-vorticity contours colored by z-velocity, showing tip vortex structure. Cartesian: Level-6, 5th Order.

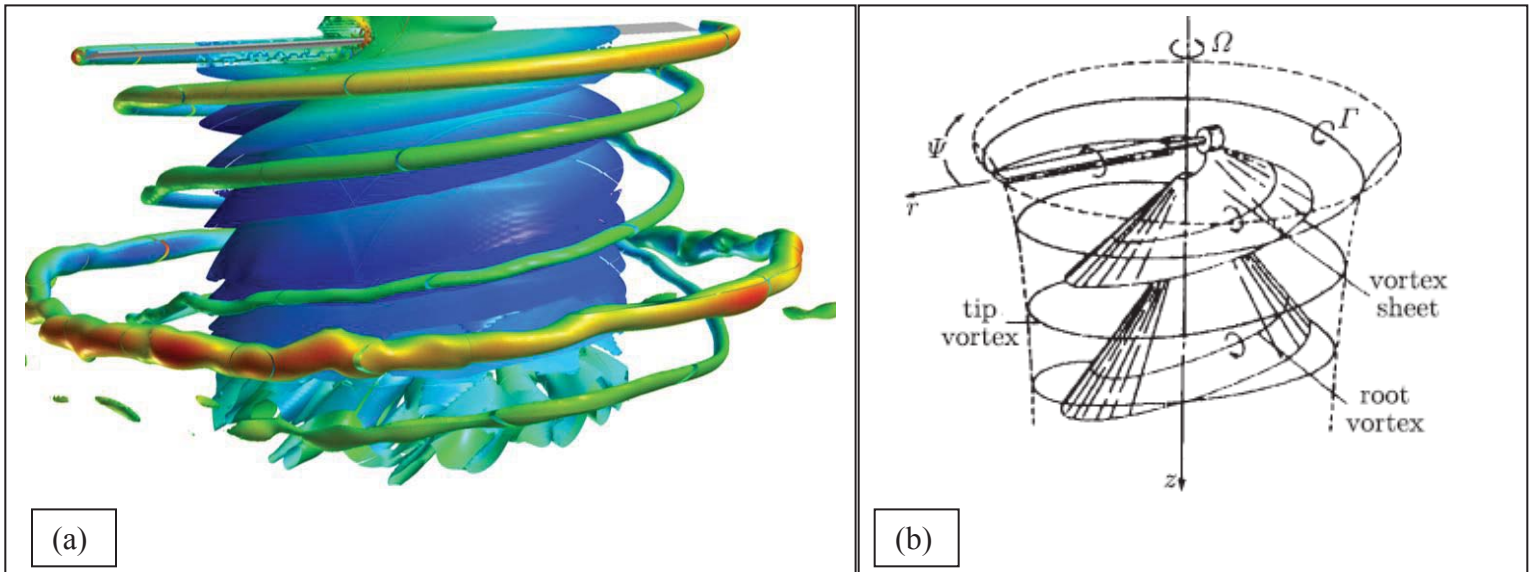


Figure 3.7. Vorticity Iso-vorticity contours colored by z-velocity, showing the helical wake structure comprising of the tip vortex, and the vortex sheet structure. Cartesian: Level-6, 5th Order.

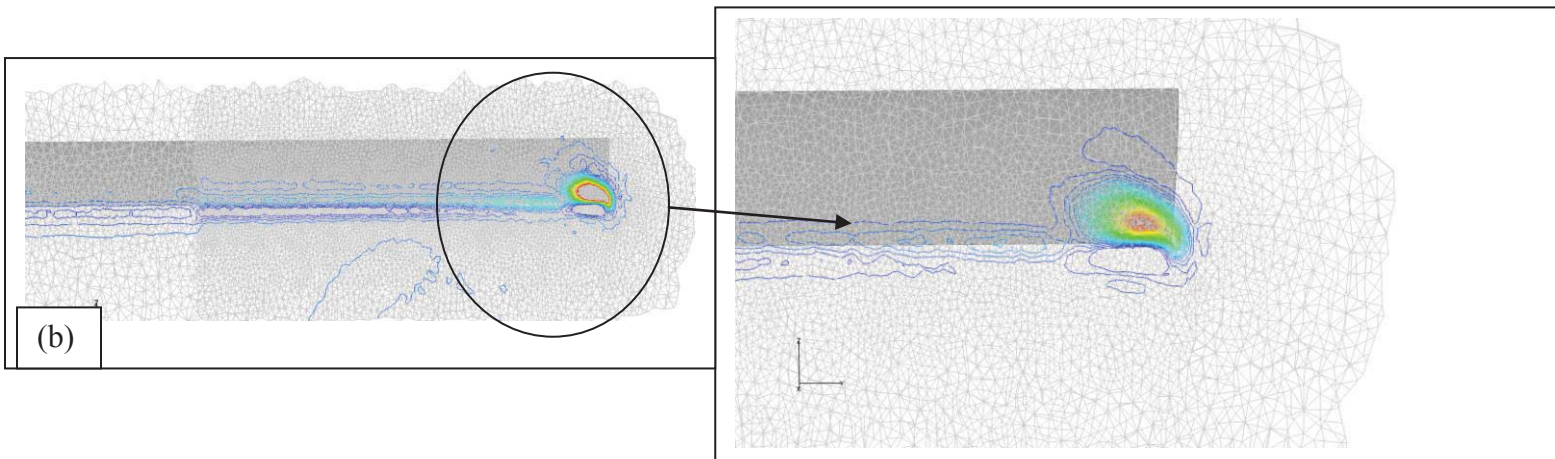
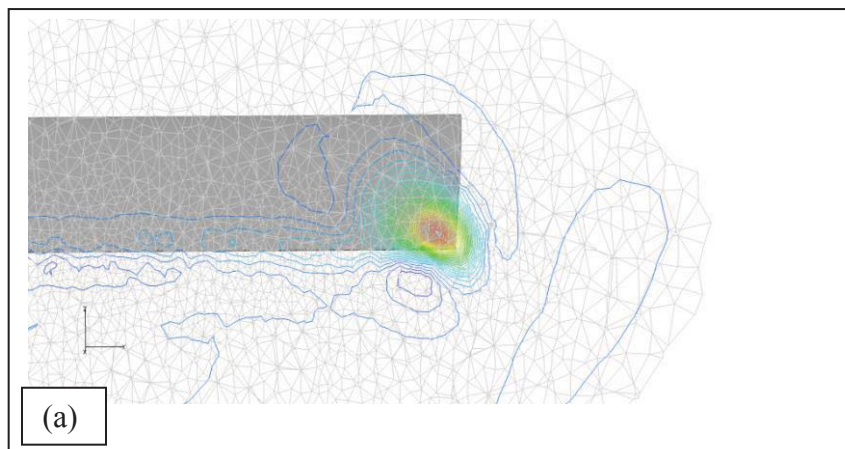


Figure 3.8 . Vorticity contours in a streamwise plane off the blade trailing edge. Solution in the near-body grid, 2nd order accuracy. (a) Level-0 grid (b) Level-1 refined grid.

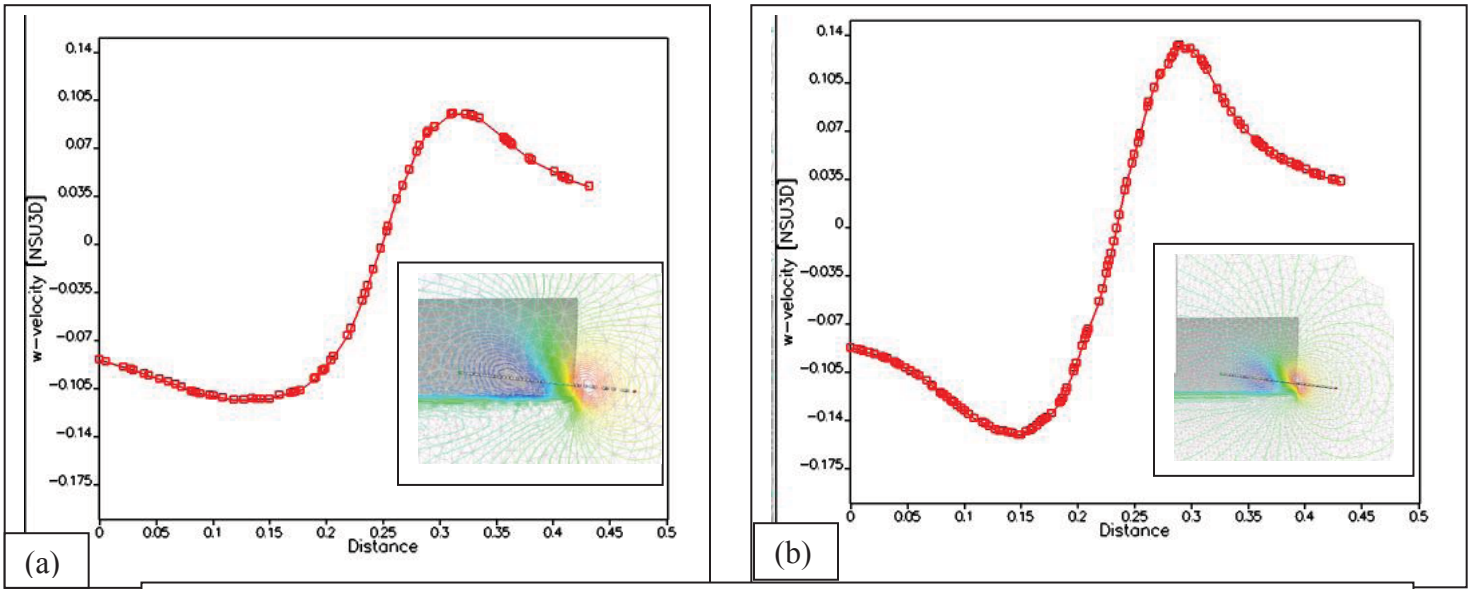


Figure 3.9. Tangential velocity profile across the tip vortex in the NBE grid (inset: w -velocity contours in a streamwise plane off the blade trailing edge). Solution in the near-body grid, 2nd order accuracy: (a) Level-0 grid (b) Level-1 refined grid.

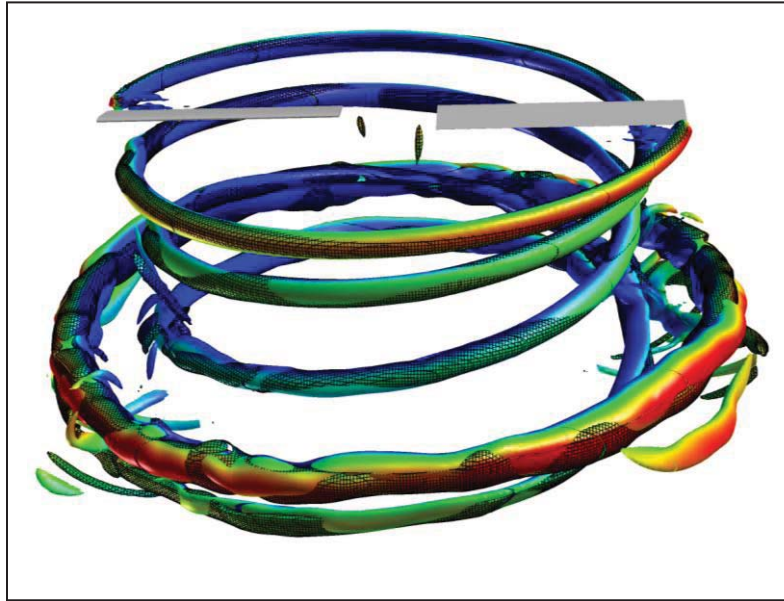


Figure 3.10. Vorticity iso-surface contours. Cartesian solutions from NBE-R0 (colored by z -velocity), and NBE-R1 (black grid lines) grids overlaid on top of each other.

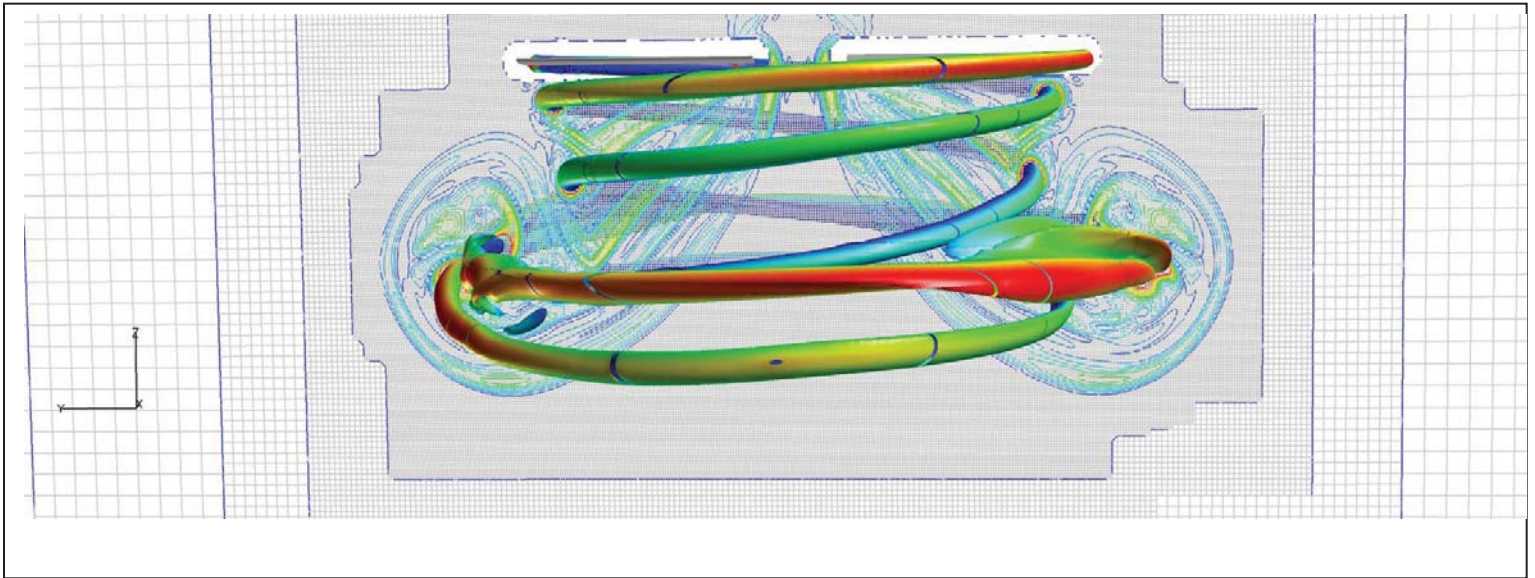


Figure 3.11 . Vorticity iso-surface contours colored by z-velocity. Automated Cartesian Mesh Refinement applied (Maximum Level-6), vorticity threshold=0.005.

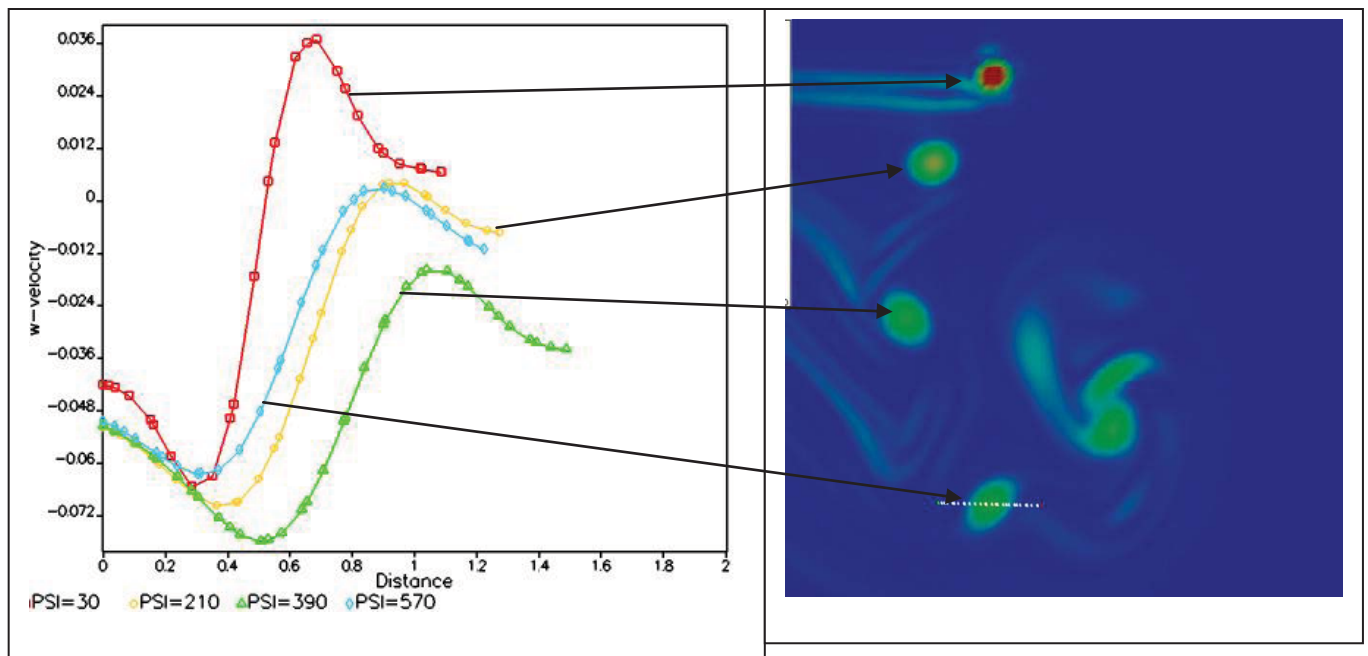


Figure 3.12. Tangential velocity profile across the wake tip vortex at several wake-age stations.

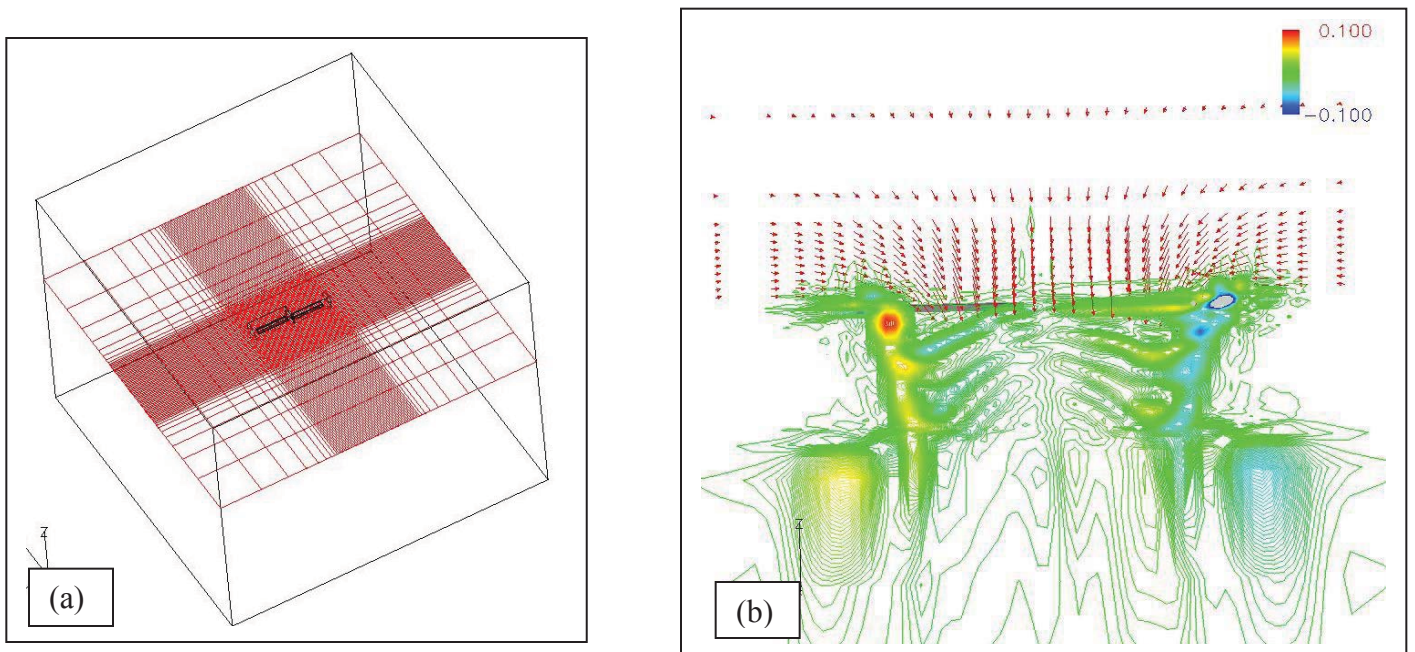


Figure 3.13. Fully high ordered structured overset simulation of the C-T rotor. Near-body C-grids, Cartesian background grid. Seventh order spatial accuracy (Hariharan and Ekaterinaris[23])

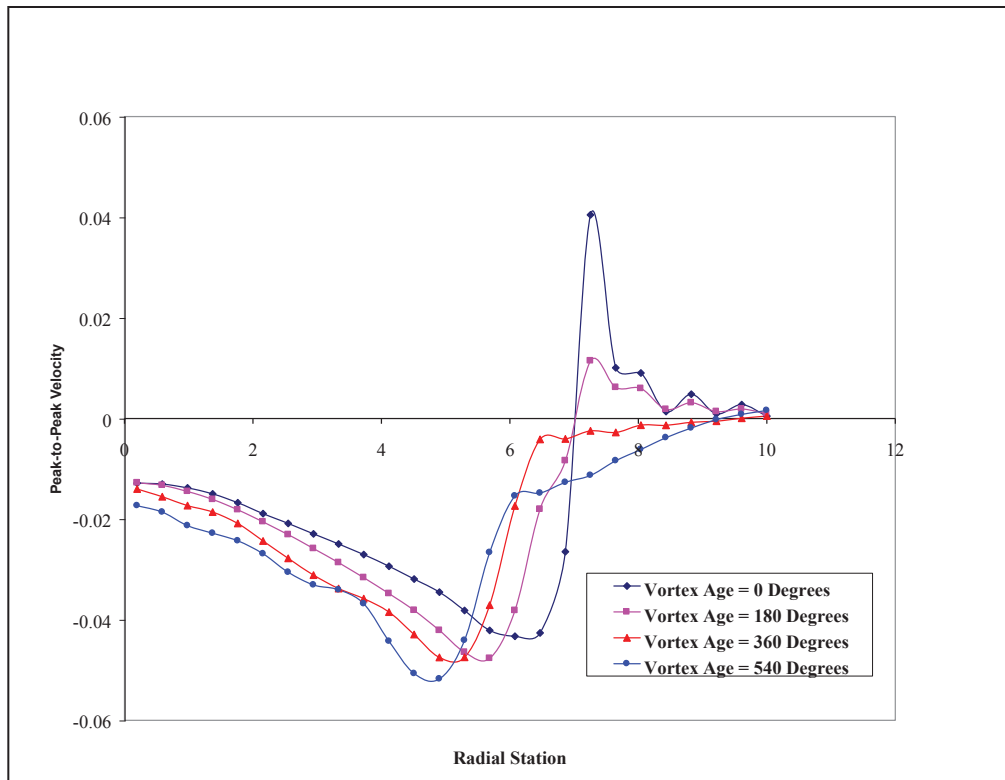


Figure 3.14. Fully high ordered structured overset simulation of the C-T rotor. Near-body C-grids, Cartesian background grid. Seventh order spatial accuracy (Hariharan and Ekaterinaris[23])

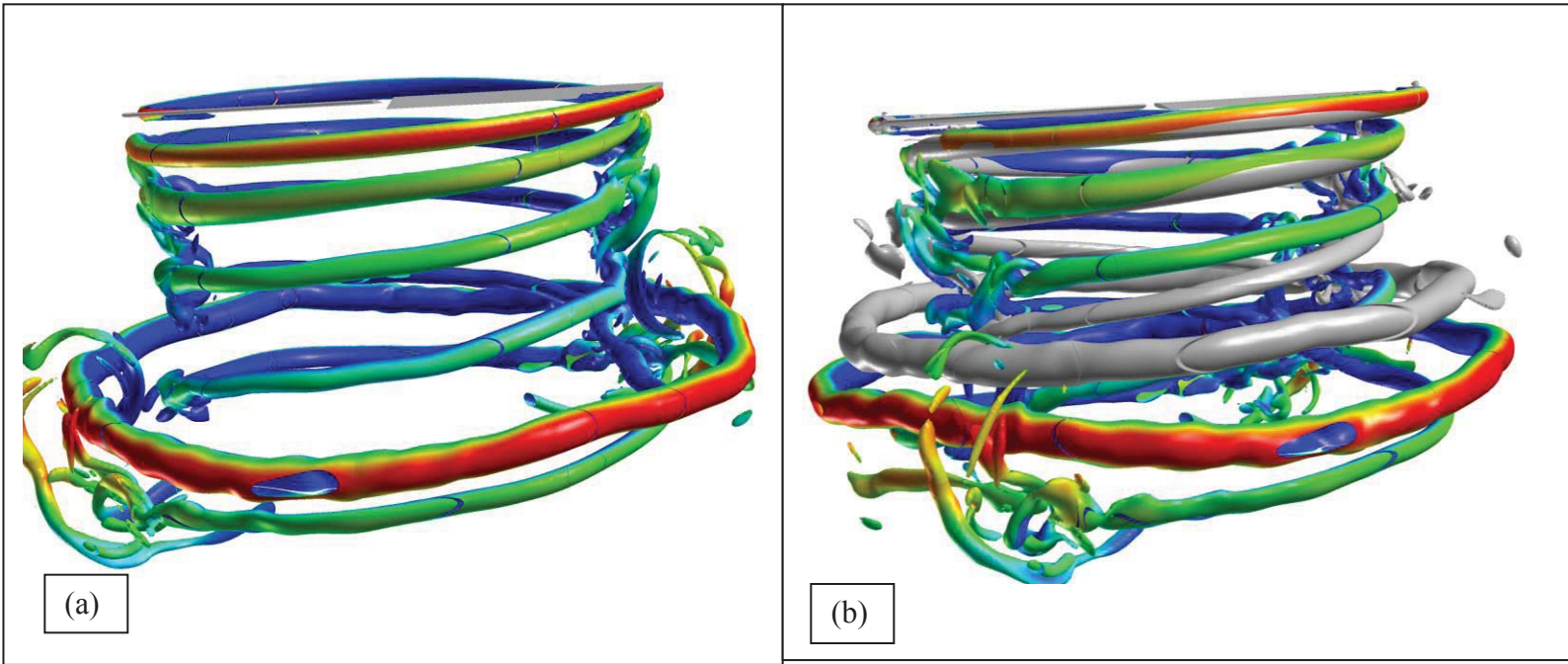


Figure 3.15 . Vorticity magnitude iso-surface colored by z-velocity. Level-6: (a) Inertial, (b) Inertial (colored by z-velocity) vs. Rotational (grey).

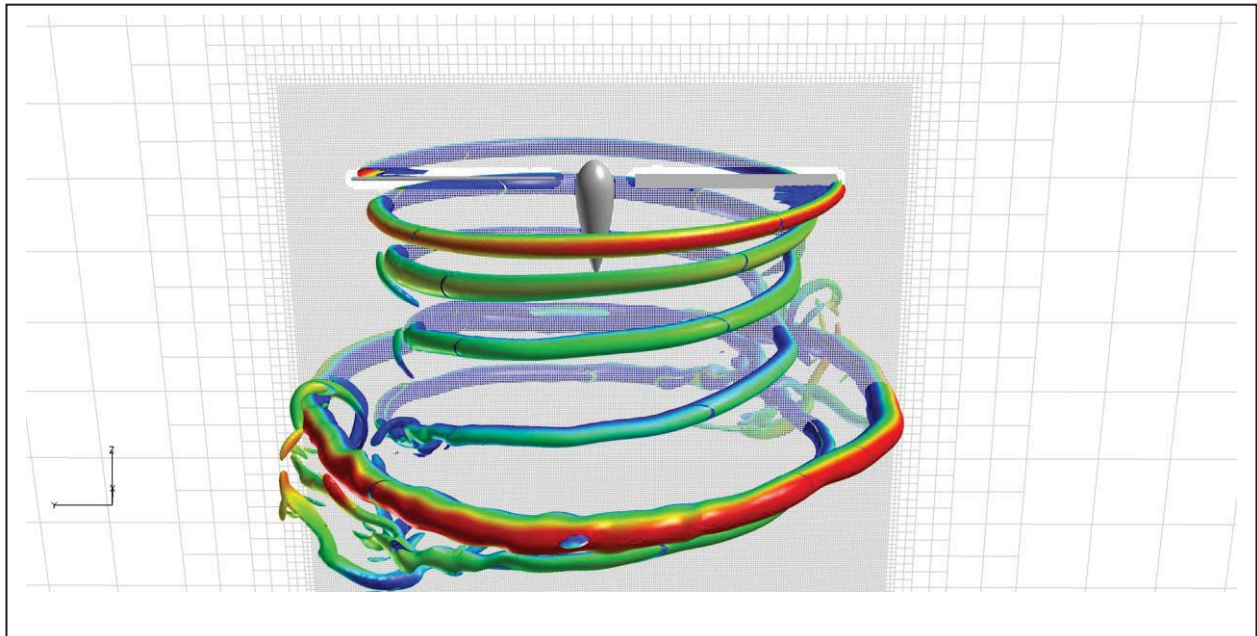


Figure 3.16 . Vorticity magnitude iso-surface colored by z-velocity. Level-6: Inertial run with a tear-drop center-body.

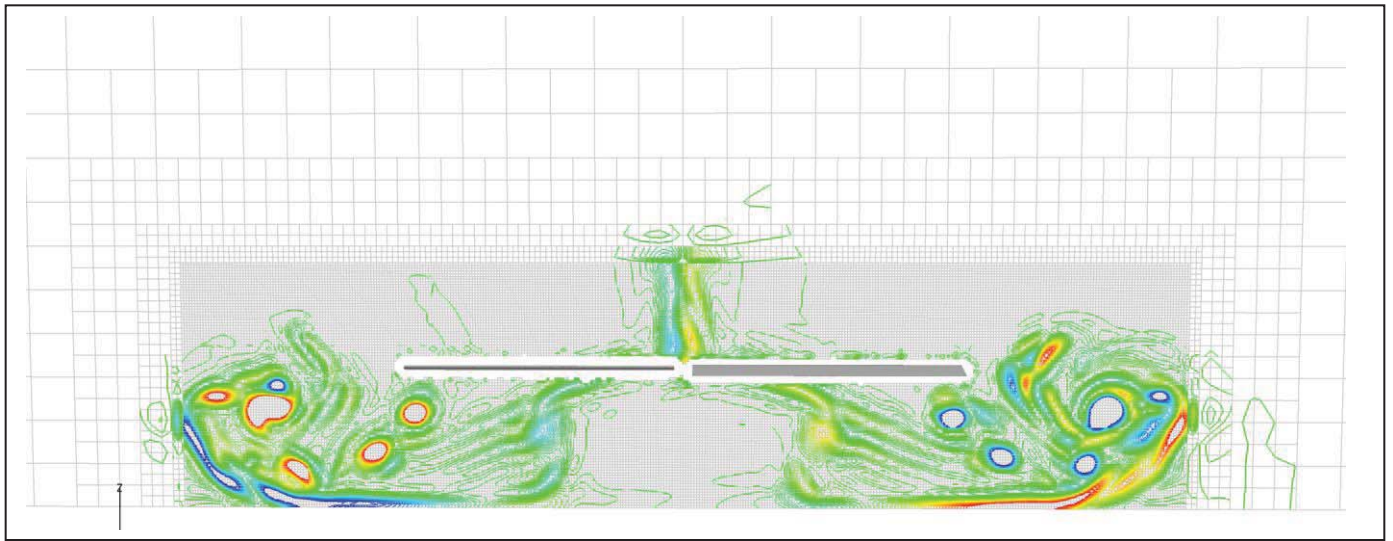


Figure 3.17. Vorticity magnitude countours. Level-6: Rotor blade hovering above ground (ground clearance=0.5 rotor radius).

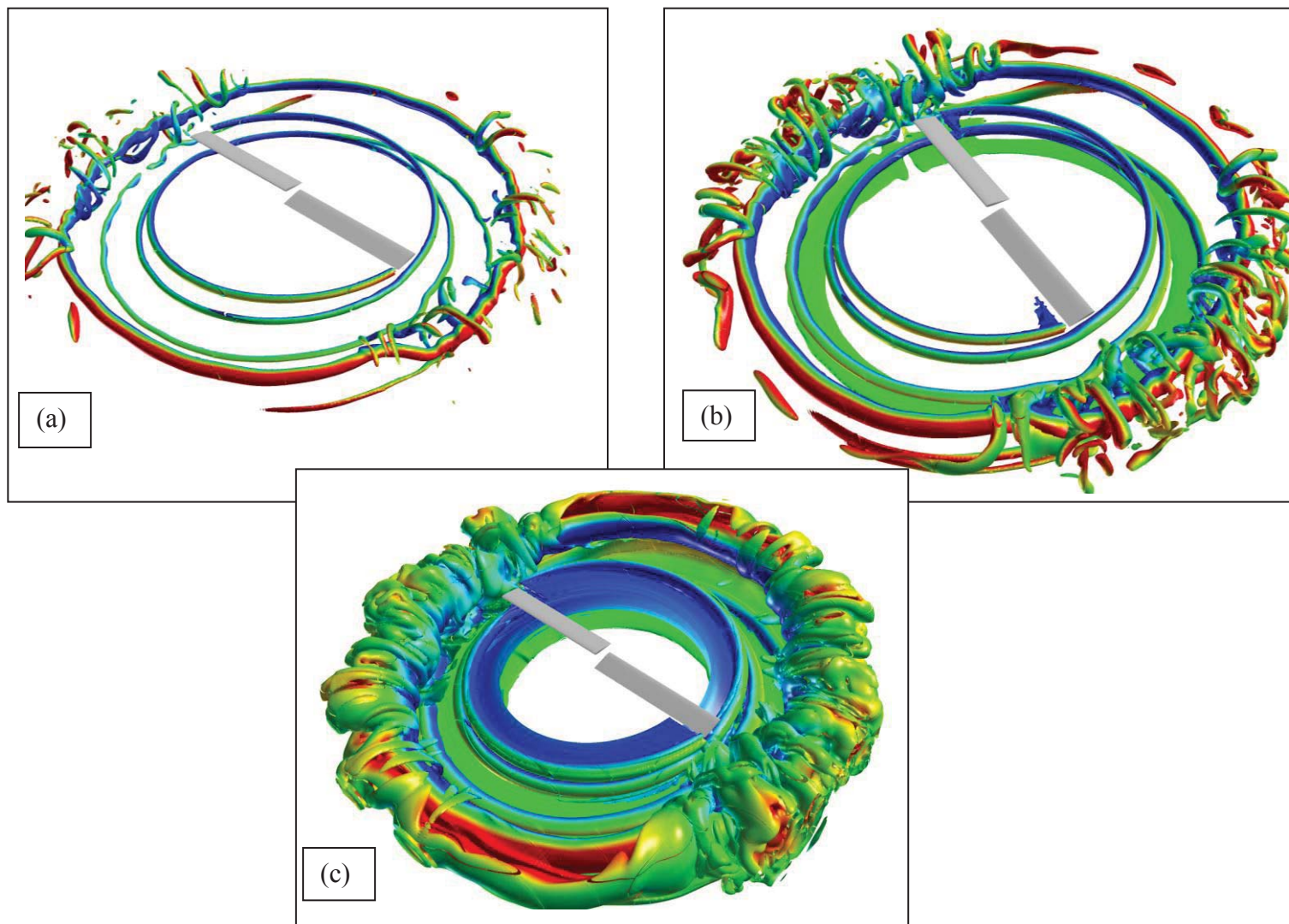


Figure 3.18 . Vorticity magnitude countours, Level-6: Rotor blade hovering above ground (ground clearance=0.5 rotor radius). (a) High level iso-surface, (b) Medium level iso-surface, (c) Low level iso-surface. Secondary vortical structures enhance mixing – aiding “Brownout” scenarios.

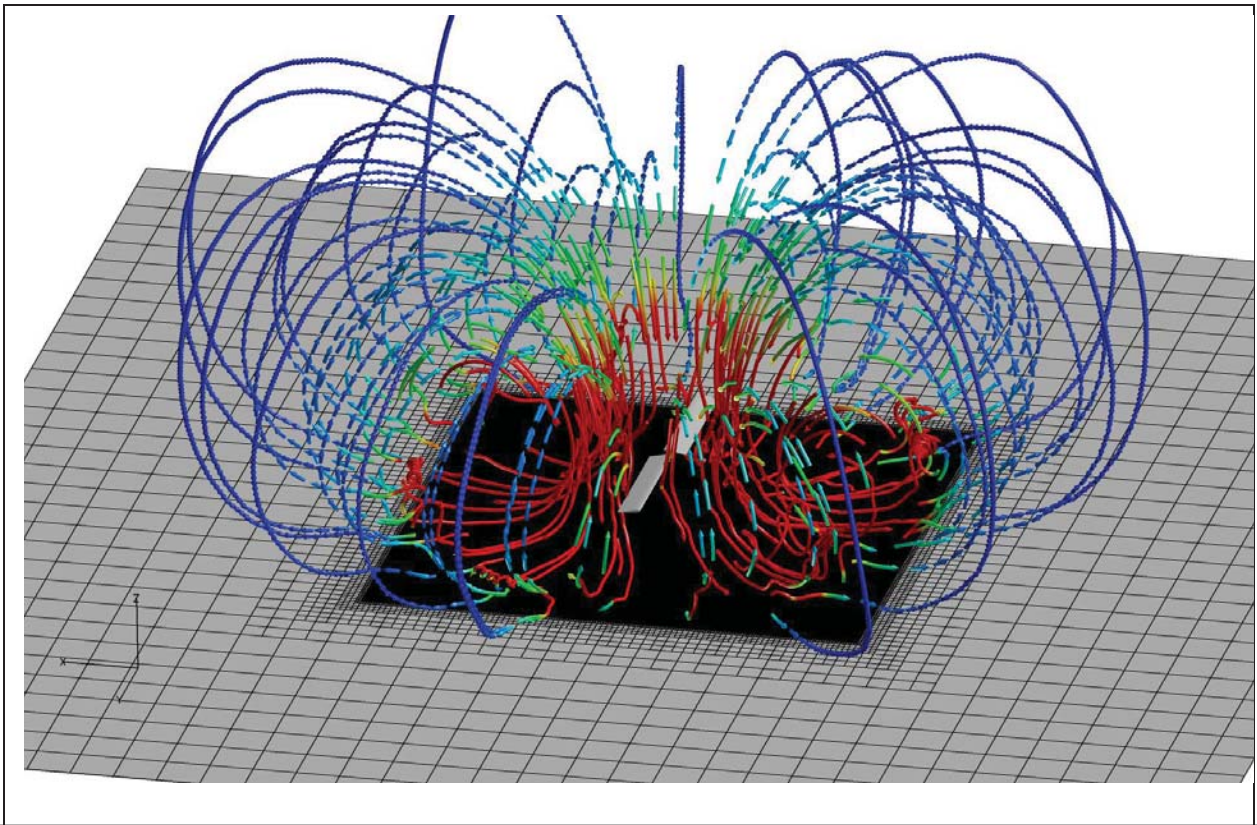


Figure 3.19 . Streamlines of particles released near the ground plane, colored by velocity magnitude (ground clearance=0.5 rotor radius). High level of mixing in the internal structures distorts the free-flight pure solenoidal field.

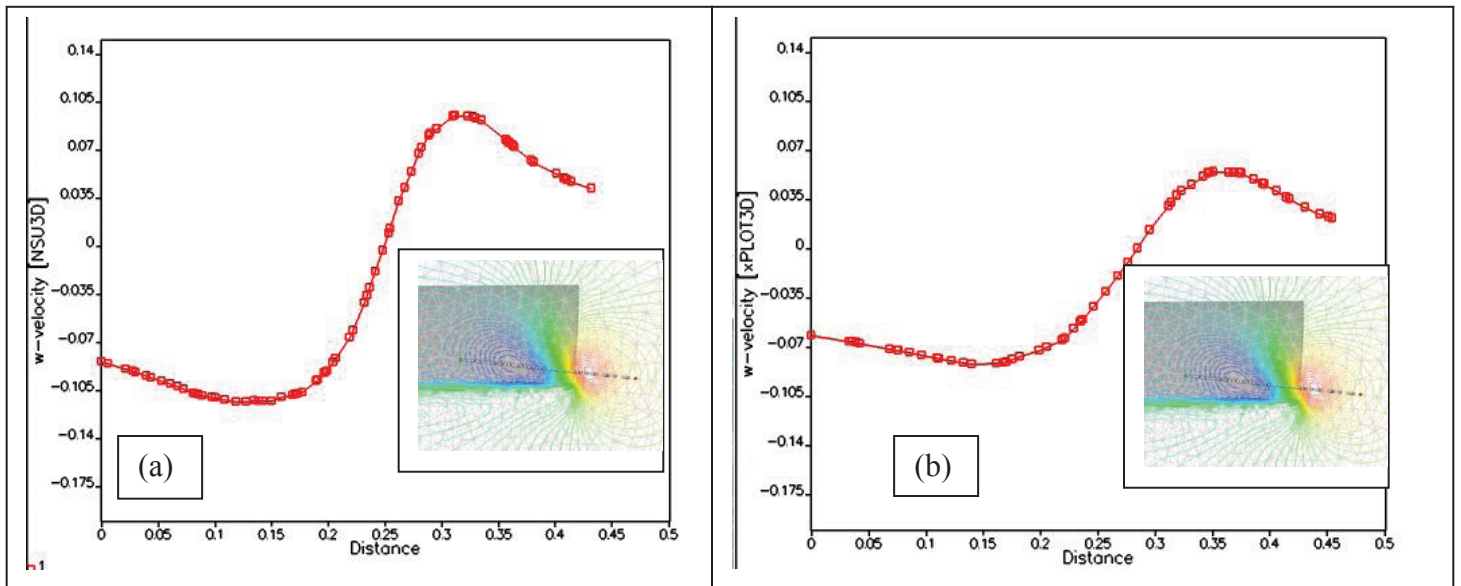


Figure 3.20 . Tangential velocity profile across the tip vortex in the NBE grid (inset: w-velocity contours in a streamwise plane off the blade trailing edge). Solution in the near-body grid, 2nd order accuracy. (a) Out-of-ground hover (b) Near-ground hover (0.5 rotor radius ground clearance).

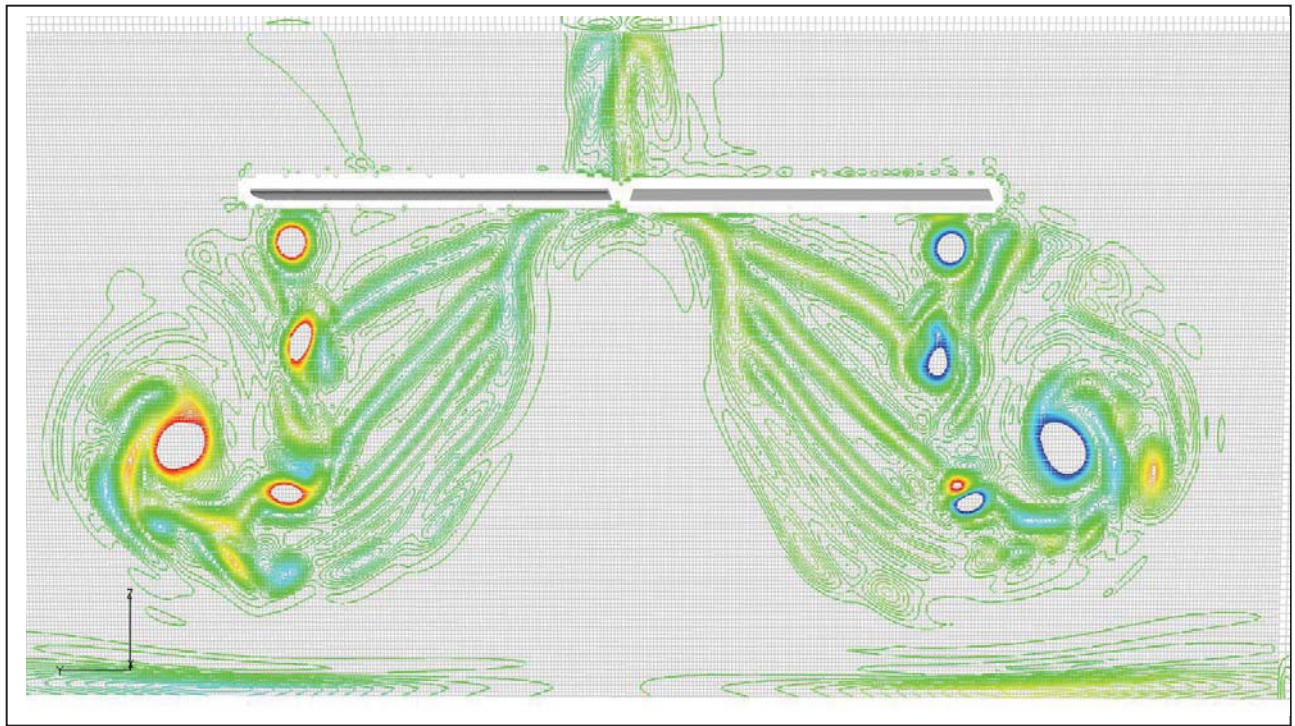


Figure 3.21 . Vorticity magnitude countours. Level-6: Rotor blade hovering above ground (ground clearance=1.25 rotor radius).

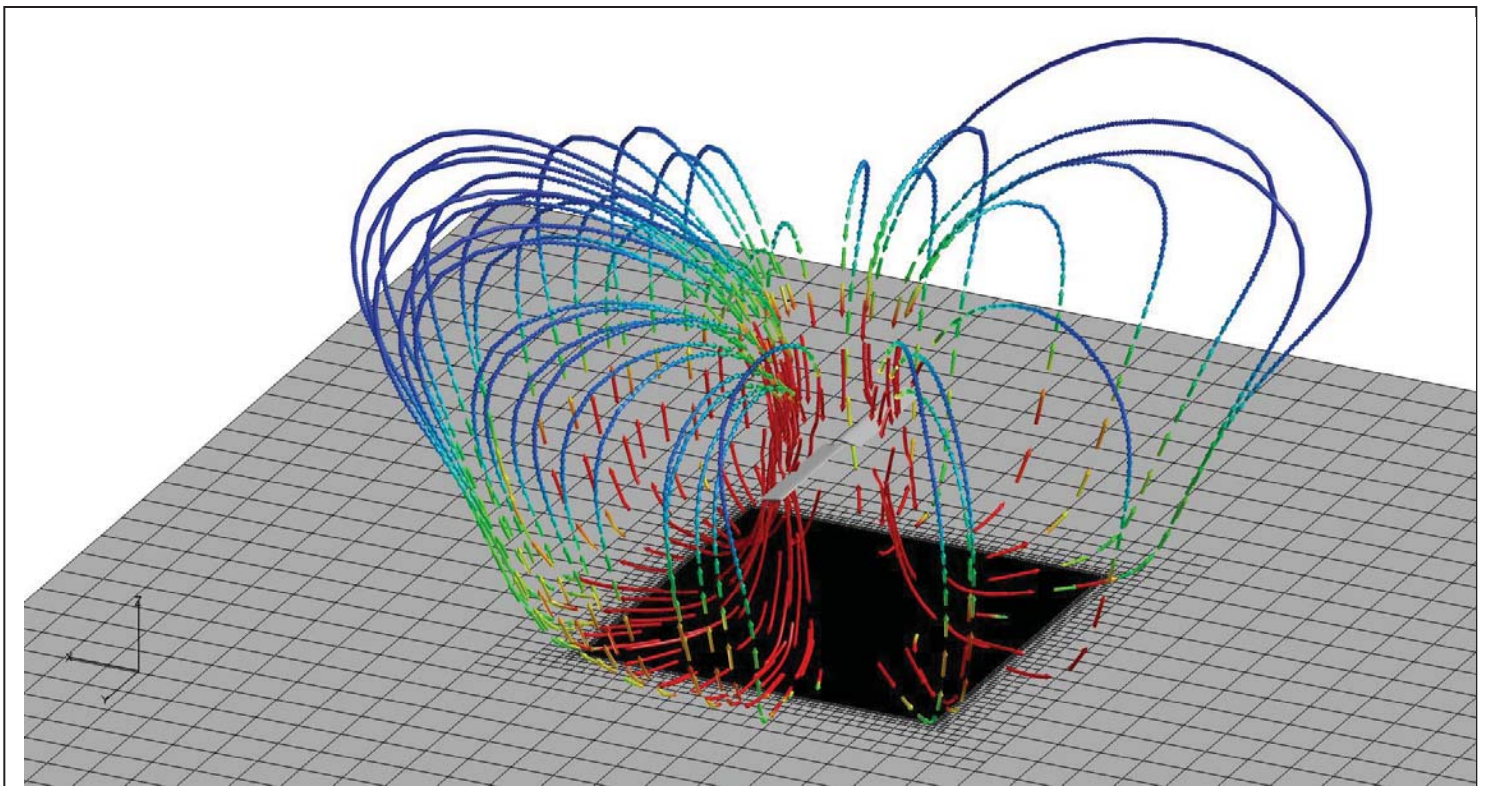


Figure 3.22. Streamlines of particles released near the ground plane, colored by velocity magnitude (ground clearance=1.25 rotor radius). Velocity field approaching free-flight pure solenoidal pattern.

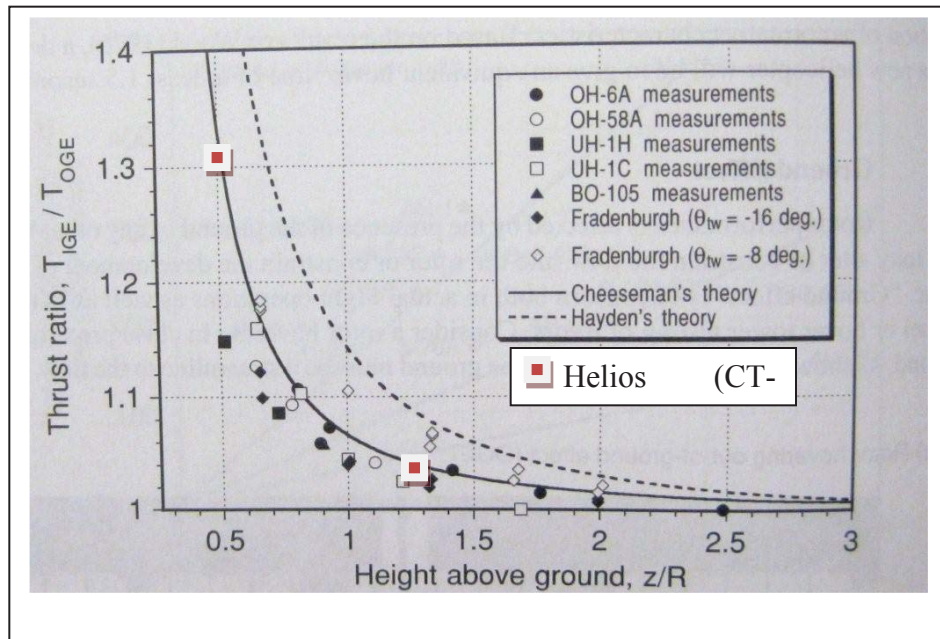


Figure 3.23. Comparison of predicted thrust gains (In-ground effect vs. out-of-ground effect) with historical data, and image-vortex theory (reproduced from Leishman[24]).